Federated Activity H_SAF_FA15_01

Cooperation on the use of combined spaceborne active and passive MW observations for precipitation retrieval

Final report

Giulia Panegrossi

Institute of Atmospheric Sciences and Climate (ISAC)
National Research Council (CNR), Rome, Italy

Mark S. Kulie

Michigan Technological University, Houghton, MI, USA
(previously at SSEC/UW-Madison, Madison, WI, USA)

Benjamin T. Johnson

Atmospheric and Environmental Research @ NOAA Joint Center for Satellite Data Assimilation (JCSDA), College Park, MD, USA

with contributions from

Daniele Casella *(SERCO, S.p.A., previously at CNR-ISAC*), **Anna Cinzia Marra** *(CNR-ISAC)*, **Jean-François Rysman** *(CNR-ISAC)*, and **Paolo Sanò** *(CNR-ISAC)*

November 24, 2017

TABLE OF CONTENTS

List of Tables

List of Figures

LIST OF ACRONYMS

AMSR-2 Advanced Microwave Scanning Radiometer-2
AMSR-E Advanced Microwave Scanning Radiometer-Earth Observing System
AMSU Advanced Microwave Sounding Unit
ATMS Advanced Technology Microwave Sounder
CDRD Cloud Dynamics Radiation Database
DMSP Defense Meteorological Satellite Program
DPR Dual-frequency Precipitation radar
EUMETSAT European Organisation for the Exploitation of Meteorological Satellites
GCOM W1 Global Change Observation Mission-Water 1
GMI GPM Microwave Imager
GPM Global Precipitation Measurement
GPM-CO Global Precipitation Measurement – Core Observatory
GPROF Goddard PROFiling algorithm
H-SAF Satellite Application Facility on support to Hydrology and Water Management
IFOV Instantaneous Field-of-View
LEO Low Earth Orbit
JAXA Japan Aerospace Exploration Agency
MetOp Meteorological Operational
MHS Microwave Humidity Sounder
NASA National Aeronautics and Space Administration
NOAA National Oceanic and Atmospheric Administration
POD Probability of Detection
PMW Passive Microwave
PNPR Passive microwave Neural network Precipitation Retrieval
SSMIS Special Sensor Microwave Imager-Sounder
TB Brightness Temperature

1. Introduction

The availability of unique observational datasets from the Global Precipitation Measurement (GPM) mission and the high level of expertise, and of the software available through the Precipitation Measurement Mission (PMM) Science Team have been recognized by H-SAF as key elements in the validation, consolidation, and upgrade of current H-SAF passive microwave (PMW) products, developed for all radiometers in the GPM constellation (SSMIS, AMSU/MHS, ATMS, AMSR-2, and GMI) during CDOP-2, and for the future products for the EPS-SG MW radiometers (MWI, MWS, and ICI) to be developed in the CDOP-3. One of the most challenging areas of development is the detection and retrieval of snowfall. The assessment of the actual observational capabilities of snowfall by spaceborne microwave radiometers is a crucial step to be able to develop and improve precipitation retrieval algorithms.

The PMM Research Program has always recognized the value in using coincident overpasses of spaceborne radars (i.e., TRMM Precipitation Radar, the Cloudsat Cloud Profiling Radar (CPR), and, now, the GPM DPR) with PMW radiometers, to evaluate the potentials, suitability, and limitations of PMW precipitation retrieval. Similarly, within H-SAF the TRMM PR and GPM DPR products have been used to assess the quality of H-SAF products over Africa and Southern Atlantic (Casella et al., 2015, and Panegrossi et al., 2014, Sanò et al., 2015, 2016). The use of spaceborne radars has the great advantage of the consistency of the observations used as reference across the world, including regions where ground-based measurements are sparse or not available.

The participation of H-SAF Team Members to the PMM Science Team, consolidated through the H-SAF-GPM collaboration proposal approved by the PMM Research Program in May 2014, has lead to the current Federated Activity (H-SAF_FA_15_01) aimed at the improvement of snowfall retrieval techniques exploiting high frequency channels present in all PMW radiometers (except in AMSR-2) in the GPM era and beyond (i.e., EPS-SG MWI, MWS, and ICI). The Federated Activity is based on the exchange of expertise between H-SAF Precipitation product development team at ISAC-CNR, and PMM Science Team members Dr. Mark Kulie [MTU, MI, USA (formerly at SSEC/UW-Madison)] and Dr. Ben Johnson [at JCSDA/NOAA since July 2015 (previously at NASA-GSFC/UMBC-JCET)]. Dr. Kulie's work in collaboration with the developers of the CloudSat snowfall product (2C-SNOW-PROFILE) at SSEC and at the UW-Madison Department of Atmospheric and Oceanic Sciences, and their expertise in snowfall retrieval have been leveraged during the FA to appropriately use CloudSat products in collaborative PMW precipitation-related activities. Moreover, Dr. Kulie, as well as other PMM Team Members, have active research projects related to rain and snowfall estimation over complex terrain, as well as shallow convective snowfall that commonly occurs in the Baltic Sea, Gulf of Finland, and Norwegian Sea. They also have precipitation remote sensing experience in observations from high latitude areas like Greenland and Antarctica that are difficult regions for PMW retrievals.

Finally, Dr. Johnson experience in the development of advanced forward radiative transfer modeling techniques, and creation of large complex-shaped frozen hydrometer databases (Johnson et al., 2010, 2016, Skofronick-Jackson and Johnson, 2011, Skofronick-Jackson et al., 2013), and Dr. Kulie experience in the assessment of the microwave scattering properties of frozen hydrometeor models and global snowfall estimation using radar and radiometer observations (Kulie et al. 2015, Kulie et al 2014, Kulie et al., 2010, Kulie and Bennartz, 2009) will be crucial to define limitations and capabilities of each passive sensor to observe snowfall and to upgrade .

Both the PMM Research Program and the EUMETSAT H-SAF will greatly benefit from this common effort, not only for the current GPM mission, but also for future climate and precipitation missions that are likely to be strongly multinational.

2. Objectives

The work during the Federated Activity (FA) has focused on the fulfillment of the following objectives:

1) to prepare observational datasets from coincident overpasses of spaceborne precipitation radars GPM DPR and CloudSat CPR to evaluate the limitations and potentials of DPR with respect to CPR in the detection and retrieval of snowfall. In order to use the GPM DPR as reference for evaluating or developing PMW products it is crucial to assess its capabilities in discriminating precipitating clouds (also at high latitudes and in presence of snowfall) for different precipitation regimes;
2) to prepare datasets from coincident overpasses of spaceborne precipitation radars GPM DPR and CloudSat CPR with PMW radiometers AMSU/MHS, AMSR-E, ATMS and GMI to relate high frequency channel observations (window and absorption band channels above 85 GHz) to the cloud and precipitation structure available from coincident spaceborne radar measurements;
3) to exploit the datasets created in 2) to define the limitations and capabilities of ATMS to observe snowfall (in particular at high latitudes) in relation to environmental characteristics (i.e., background surface and integrated water vapor content). It is worth noting that ATMS is the most advanced cross-track scanning radiometer currently available, precursor of the future MWS on board the EPS-SG series;
4) to extend the GMI/CPR coincident dataset to include ancillary data useful to analyze the snowfall observational capabilities of GMI. It is worth noting that GMI is the most advanced conically scanning radiometer currently available and useful insights can be obtained about the potential and limitations of MWI on board the EPS-SG series;
5) to develop a prototype algorithm for snowfall detection based on the finding of 4);
6) implementation of a new methodology to infer the optical properties of ice cloud, using not-spherical ice single scattering table made available by the PMM Science Team, starting from the CPR reflectivity profile.

The work carried out during the FA has contributed to define the strategy for the development of new snowfall retrieval techniques the EPS-SG MWI and MWS day-1 products through the use of the observational datasets and through the refinement of the physical assumptions in the retrieval algorithms.

The results of 1), 2) and part of 3) have been presented in the Mid Term report. In this Final Report the results of 4) and 5) for the GMI are presented in Section 6 and 7. The work related to 8) carried out within this Federated Activity and future developments in the framework of the on-going collaboration between H-SAF and GPM are presented in Section 8.

3. Logistics

The FA kick-off meeting has been held on July 15, 2015 during the PMM Science Team Meeting 2015, Baltimore, MD. The Participants were Dr. Giulia Panegrossi and Dr. Daniele Casella (ISAC-CNR) Dr. Mark Kulie (SSEC/UW-Madison) and Dr. Ben Johnson (at NOAA since July 2015). A short-term visit of Dr. Panegrossi at SSEC/UW-Madison following the meeting has been an excellent opportunity to define the activities and strategies related to objectives of the FA. During the summer 2015, Dr. Casella visited Dr. Kulie at SSEC/UW-Madison (2 month visit) to work on the preparation of DPR/CPR, ATMS/CPR and GMI/DPR/CPR coincidence datasets, and to develop a frozen surface type classification algorithm based on PMW observations (the proper characterization of the background surface is crucial to determine the snowfall detection capabilities of PMW sensors). The activity in 2016 focused on the definition of the limitations and capabilities of DPR and of the most advanced cross-track scanning radiometers, the ATMS, to observe snowfall in relation to environmental conditions, using CloudSat snowfall products as reference (objectives 1 to 3). The results of this activity have been reported in the FA Mid Term Report delivered in December 2016, and in peer-reviewed paper (Casella et al., 2017). In 2017 the activity focused on the analysis of GMI capabilities to observe snowfall (objective 4 and 5). The results of the analysis of GMI snowfall observational capabilities have also been collected in a scientific paper (Panegrossi et al., 2017) recently submitted for publication. During this time frame, continuous interactions with Dr. Mark Kulie via teleconferences, and his short-term visit to CNR-ISAC in June 2017 (sponsored by the CNR Short Term Mobility program 2016) have contributed to the achievement of significant scientific results presented in this Final Report. The interactions with Dr. Kulie during this FA have also contributed to the upgrade of the

radiative transfer code and single scattering tables currently used in the H-SAF precipitation product development (objective 6).

4. Scientific Background

Snowfall detection from space using passive microwave (PMW) observations is extremely challenging. Two main obstacles are encountered by PMW snowfall retrieval schemes: i) the inability to reliably distinguish the respective falling snow and background surface contributions to the upwelling radiation from the earth/atmosphere system (e.g., (e.g., Skofronick-Jackson and Johnson 2011; You et al. 2016) and ii) the quantitative precipitation estimation uncertainties related to varying and ill-constrained ice/snow microphysical properties that obfuscate high microwave frequency ice/snow particle scattering signatures (e.g., Kulie et al. 2010). High latitude surfaces are also frequently (or permanently) snow or ice-covered with elevated and variable surface emissivities (Prigent et al. 2006; Turk et al. 2014), thus rendering the solid precipitation contribution to upwelling microwave radiation difficult to isolate from the surface contribution. This issue is further magnified by the relatively subtle PMW signal associated with low precipitation rates (Kongoli et al., 2015). Various studies have shown that extremely light snowfall rates dominate the snowfall rate distribution at higher latitudes (Liu 2008; Kulie and Bennartz 2009; Kulie et al. 2016).

Microwave sensors with high-frequency channel diversity offer a unique opportunity for significant advances in surface snowfall retrievals. It is worth noting that the lengthy legacy microwave radiometer imager precipitation data record collected by such instruments as the Special Sensor Microwave Imager (SSM/I), the Tropical Rainfall Measuring Mission (TRMM) Microwave Imager (TMI), and the Advanced Microwave Scanning Radiometer-EOS (AMSR-E) included microwave channels up to 85/89 GHz. The 85/89 GHz channels are considered high-frequency microwave channels with demonstrated ice scattering sensitivity associated with tropical and mid-latitude rain events (e.g., Spencer et al, 1989; Bennartz and Petty 2001). These channels on microwave imagers that employ fixed oblique observation angles can be especially useful for oceanic precipitation rate retrievals by exploiting high-frequency polarization signals. Tools that exploit polarization information have been developed to isolate the ice scattering brightness temperature (TB) signature at higher microwave frequencies from highly polarized oceanic background (e.g., the Petty (1994) scattering index), The 85/89 GHz channels, however, are too sensitive to the surface at higher latitudes, where the atmosphere opacity is lower, for consistently effective snowfall retrieval, especially over land surfaces (Skofronick-Jackson and Johnson 2011). This is why higher frequency "window" channels located in 150-170 GHz range, combined with observations utilizing gaseous absorption features between 100-200 GHz, are now privileged for snowfall detection since they respond more effectively to ice microphysics compared to 85/89 GHz channels (e.g., Liu 2008; Kulie et al. 2010; Kuo et al 2016; Olson et al. 2016). More importantly, these higher frequency channels – including the so-called "window" channels - are less prone to surface effects because the opacity (transmissivity) of the atmosphere increases (decreases) as the microwave frequency increases (due to water vapor continuum or oxygen absorption) (Skofronick-Jackson et al. 2004). In dry conditions, however, the contribution of the surface to the upwelling radiation at these frequencies can be quite significant. Current microwave imagers such as the Global Precipitation Measurement (GPM) Microwave Imager (GMI), combination microwave imager/sounders (e.g., Special Sensor Microwave Imager and Sounder (SSMIS)), and microwave sounders (e.g., Advanced Technology Microwave Sounder (ATMS)) offer high-frequency channel assortment that can be used for snowfall detection and quantitative precipitation retrievals.

Theoretical modeling studies demonstrate the potential of high-frequency channel combinations for snowfall detection purposes (e.g., Bennartz and Bauer 2003; Di Michele and Bauer 2006). While oceanic snowfall rate estimation using high-frequency channels should hypothetically be a tractable retrieval scenario due to a fairly well-behaved and understood surface background, the results by (Skofronick-Jackson and Johnson 2011) indicate complexities over land surfaces. They demonstrated that higher frequencies (e.g., 166 GHz and 183.3 GHz channels) are more sensitive to frozen hydrometeor scattering and partially mask the surface contribution, but with varying degrees of sensitivity depending on the ice water path and atmospheric moisture profile associated with each snowfall regime. They also highlight the

difficulties associated with isolating the snowfall signal at higher microwave frequencies due to complex interaction between surface and atmospheric features that determine the multi-frequency TB signal. Recent work by Ebtehaj and Kummerow (2017) using GMI data, however, illustrates that snowfall detection may be possible over land with no snow cover by using combined 10 and 166 GHz horizontal polarization channel information, while 89 GHz horizontal polarization observations provide crucial information for snow-covered surfaces.

Other studies have been carried out to analyze snow scattering signals and the effect of snow particle orientation on polarization differences observed with a ground-based radiometer (e.g., Kneifel et al., 2010, Xie et al., 2012). In the work by Kneifel et al. (2010) a significant TB enhancement in ground-based measurements at 90 and 150 GHz is observed in presence of snowfall, due to the large amounts of liquid water and to the presence of supercooled droplets often found for the snowfall cases analyzed. The study by Xie et al. (2012) shows that the polarization difference at 150 GHz can be explained by the occurrence of oriented snow particles, and that while high snow water path enhances polarization differences, the presence of supercooled water damps the polarization differences, and enhances the TBs. These studies support the potential role of polarization measurements for improved retrievals of snowfall microphysical parameters, and the importance of accurate modeling of the radiative properties of supercooled water for snowfall retrieval algorithms using high microwave frequencies. Moreover, the work by Kneifel et al. (2010) evidences the need of studies on the use of passive measurements at frequencies higher than 150 GHz combined with radar systems (above 35 GHz) to test their potential for snowfall detection and retrievals.

The application of high-frequency channels using 150 and 183.3 GHz spaceborne microwave sounder channels – more specifically, using TB differences from channel pairs with weighting functions that peak at different atmospheric levels - has also been shown in proof-of-concept snowfall detection studies and snowfall product development (Kongoli et al. 2003; Surussavadee and Staelin 2009; Noh et al. 2009; Kongoli et al. 2015). For example, the work by Noh et al. (2009) illustrates United States Laurentian Great Lakes snowfall retrieval potential using previous generation operational microwave sounder data from the Advanced Microwave Sounding Unit (AMSU-B). They noted generally positive results, especially in the early winter season when sustained ground snow cover is limited. In later winter months, however, snowfall retrievals using sounding channels were susceptible to snow-covered ground contamination. Enhanced screening methods that account for seasonal surface differences can significantly reduce false detections (Kongoli et al. 2015).

High-frequency microwave channels and surface effects are important factors to consider for the current GPM mission. Studies that systematically assess the information contained in various GMI channel combinations for snowfall detection have been undertaken in recent years using spaceborne radar observations to identify snowfall events globally. For instance, in the work by You et al. (2016) a coincident GMI and GPM Dual-frequency Precipitation Radar (DPR) database is analyzed to determine optimal channel combinations for snowfall detection over land. Low frequency channels obviously demonstrate little information due to a weak ice scattering response. Including high-frequency channels near the 183.3 GHz water vapor absorption line contributes valuable information, but adding the 166 GHz channel to a multi-frequency channel combination is deemed optimal for snowfall detection using a GMI-like sensor. The 166 GHz channel amplifies ice/snow scattering sensitivity lower in the atmosphere, yet appropriately dampens surface influences and increases snowfall detection statistics when compared to radar-derived snow/no-snow statistics. The possible combination of high-frequency microwave channel responses to different snowfall scenarios, however, deserves further investigative attention.

The importance of high-frequency microwave radiometer observations to better understand ice scattering signatures is further illustrated by Gong and Wu (2017), whereby systematic polarized high-frequency signatures are associated with cloudy GMI observations on a global scale. In the work by Gong an Wu (2017) it is evidenced that the 89 and 166 GHz polarimetric measurements contain ample information regarding frozen particle habit and orientation. The TB differences (ΔTB) between vertically (V-pol) and horizontally (H-pol) polarized 89 and 166 GHz channel observations are found to be positive, with a distinctive bell-shaped ΔTB curve as a function of V-pol TB that peaks near 10 K for both channels. The ΔTB values are positive because of stronger H-pol extinction under cloudy conditions that may contain significant columnar liquid water and ice paths. In the study by Gong an Wu (2017), however, note that cold-season high latitude ΔTB-TB relationships are more complex than the generally invariant low latitude

ΔTB-TB relationships. This ΔTB-TB latitudinal discrepancy is most likely related to lower water vapor contents in winter atmospheres at higher latitudes, thus allowing surface influences to complicate the ΔTB signal. Conversely, the ΔTB signal can be dampened at lower latitudes due to elevated TPW amounts. The study by Gong an Wu (2017) motivates the need to investigate ΔTB-TB relationships at higher latitudes, especially 166 GHz (V-H) TB differences (hereafter 166 ΔTB) behavior in the presence of surface snowfall observed by radar with increased sensitivity compared to the DPR.

Compiling and exploiting other coincident spaceborne active and passive microwave sensor datasets will further enhance our understanding of high frequency microwave snowfall detection capabilities. This study therefore illustrates snowfall signatures over different surface classifications using GMI channel combinations and coincident CloudSat snowfall retrievals. CloudSat sensitive Cloud Profiling Radar (CPR) has proved extremely valuable for global snowfall research (e.g., Liu 2008; Kulie et al. 2009; Boening et al. 2012; Behrangi et al. 2016; Kulie et al 2016).). Combined GMI and CloudSat observations can be exploited to study radiometric signals associated with a broader range of the snowfall rate spectrum compared to the GPM DPR since the effective ~12 dBZ GPM DPR sensitivity threshold limits its effectiveness to detect lighter snowfall events (Casella et al., 2017).

5. GMI-CPR Dataset Description

This study is based on the use of co-located observations by the CPR on board the CloudSat and by the GMI on board the NASA/JAXA GPM Core Observatory. CloudSat has been operational since 2006 as part of the Afternoon Constellation (A-Train) (L'Ecuyer, and Jiang, 2010) of independent satellites flying in a formation pattern, and it follows a near-polar orbit (maximum latitude near 82°) with a 16-day overpass revisit cycle. Since 2011 CPR operates in daylight-only mode due to a battery anomaly. CloudSat has provided valuable data for the precipitation remote sensing community, especially as the first spaceborne radar to provide observations at higher latitude. The near global coverage (up to ~82° latitude) and high CPR sensitivity (~ -28 dBZ) make it very suitable for snowfall-related research (i.e., Berhangi et al., 2016, Liu, 2008, Kulie and Bennartz, 2009, Kulie et al., 2016, Palerme et al., 2014, Wang et al., 2013, Milani et al., 2017). The CPR nominal footprint size is ~1.5 km with ~480 m native vertical range gates in each reflectivity profile collected over a 0.16 s integration time interval. Due to oversampling, CloudSat products are available at ~240 m vertical intervals.

The GMI is the most advanced microwave conically scanning radiometer in space, in terms of both channel frequency assortment and spatial resolution. It offers the most appropriate set of microwave frequencies for precipitation retrieval, with 10 dual-polarization window channels from 10 GHz to 166 GHz, and three single-polarization water vapor absorption channels (at 23.8 GHz and two at 183.3±3 GHz, and 183.3±7 GHz). Moreover, GMI provides PMW measurements on a 904 km wide swath at the highest available spatial resolution, ranging from 4.4 km x 7.2 km at the high-frequency channels (> 89 GHz), to 19 km x 32 km at 10 GHz.

The GMI-CPR coincidence dataset is built starting from the NASA 2B-CSATGPM product of coincident CloudSat/GPM observations (Turk, 2016) made available through the NASA Precipitation Processing System (PPS), within the Precipitation Measurement Missions (PMM) Research Program. This product is made of coincident segments of CPR co-located reflectivities and GMI TBs within a time interval of 15 minutes or less. For the pixels located within GPM DPR swaths, centered in the GMI swath (245 km and 120 km wide for the Ku- and Ka-band radar, respectively) the datasets store DPR reflectivity profiles (measured and corrected). The GMI-CPR database used in this study includes all coincident observations available from March 2014 through the end of May 2016 (no CPR snowfall products were available after this date at the time this study was carried out).

Additional GPM, CloudSat products and ancillary data have been added to the initial dataset for this study and in view of future further applications. Precipitation profiles, and surface precipitation variables from the NASA 2A-GPROF (Kummerow et al., 2015) and 2B-CMB products (V4 and V5) (Grecu et al., 2016) and the JAXA GPM 2A-DPR (V4 and V5) Iguchi et al. (2016) have been included in the dataset. In addition, the CloudSat 2C-SNOW-PROFILE (hereafter, 2C-SNOW), used extensively in this study, provides profiles of instantaneous liquid equivalent surface snowfall rate retrievals based on CloudSat orbital swath data. The 2C-SNOW product uses an optimal estimation procedure to extract snowfall rate from W-band radar

reflectivity values, using a priori snow microphysical properties to constrain snowfall rate retrievals (Wood et al., 2013, 2014). It is worth noting that 2C-SNOW surface snowfall rate (and associated SWC profile) is computed only for CPR profiles where the 2C-PRECIP CPR product indicates surface snow probable or certain, or if estimated liquid fraction is < 10% (dry snow). These conditions are defined by considering interpolated ECMWF model temperature profiles at the near-surface clutter-free bin, and therefore are subject to the uncertainty of the model and to the ground clutter conditions (see also Milani et al., 2017). Moreover, the SWC is available only at or above the first clutter-free bin and the retrieval is provided only if the equivalent radar reflectivity factor at the first clutter-free bin is above -15 dBZ. Numerous studies have demonstrated that the CPR snowfall rates are possibly biased under different meteorological or geographical circumstances (e.g., Hiley et al., 2011, Chen et al., 2016). Exhaustive 2C-SNOW algorithm descriptions are also provided by Berhangi et al (2016) and Kulie et al. (2016). All coincident segments for which the 2C-SNOW provides a valid near-surface snowfall rate (at least in some part of the segment) have been selected for the snowfall-only dataset used in this study. In the GMI-CPR dataset used in this study, all snow related variables [i.e., snow water content (SWC), snow water path (SWP)] refer to falling snow, i.e., CPR profiles with 2C-SNOW surface snowfall rate larger than 0.0 mm h^{-1}.

Source	Sensor/ Model	Product	Main Variables
GPM	GMI	1C-R V5A	Brightness temperatures (TBs) [K}
GPM	GMI	GPROF V4 and V5	Surface precipitation rate [mm h^{-1}] Liquid fraction (V4) [%] Frozen precipitation rate (V5) [mm h^{-1}]
CloudSat	CPR	2C-SNOW-PROFILE V4	Equivalent radar reflectivity factor (Z) [dBZ] Snow water content (SWC) [kg m^{-3}] Surface snowfall rate [mm h^{-1}]
CloudSat	CPR	2C-PRECIP-COLUMN V4	Surface precipitation rate [mm h^{-1}] Liquid fraction [%]
CloudSat	CPR	2B-CLOUD-CLASS V4	Surface type Cloud type
CloudSat	ECMWF	ECMWF-AUX V4	2 m temperature (T_{2m}) [K} Surface pressure [hPa] Total precipitable water (TPW) [kg m^{-2}]
Icare/ University of Lille 1	CALIPSO/ CPR	DARDAR	Ice water content (IWC) [kg m^{-3}] Phase/microphysics classes
University of Bremen	AMSR2	ASI	Daily sea-ice concentration [%]

Table 1. List of products available in the dataset built from coincident GMI/CloudSat observations (10 March 2014 - 31 May 2016) and list of the main variables used in this study.

Another product added to the original 2B-CSATGPM dataset is the CloudSat DARDAR (liDAR+raDAR) product (http://www.icare.univ-lille1.fr/projects/dardar). It is derived from combined CPR and CALIPSO lidar measurements using a variational approach (Delanoë and Hogan 2008, 2010). The DARDAR product supplies the following ice cloud property retrievals: ice water content (IWC), ice particle effective radius, and extinction. These ice properties are provided with a vertical (horizontal) resolution of 60 m (1.7 km). The DARDAR product also provides the predominant particle phase/microphysics composition or constituent classification of each vertical bin in the following 11 classes: ground, unknown, clear, ice, ice and supercooled water, liquid warm, supercooled water, rain, aerosol, possible insect, or stratospheric feature. The assessment of the quality of DARDAR product performed by Delanoë and Hogan (2008, 2010)

against real and simulated ice profile, shows that DARDAR tends to overestimate IWC (from a few % to 30-40 % depending of the altitude of the ice). Hereafter, all ice related variables [i.e., ice water content (IWC), or ice water path (IWP)] will refer to the DARDAR product cloud ice, which include upper level clouds, thin ice clouds, as well as falling snow.

In addition, ancillary daily snow cover fraction (MOD10C1and sea-ice concentration (Arctic and Antarctic Sea-ice concentration (ASI) product from AMSR2, both at 0.05°, have been added to the dataset. It is worth noting, however, that the MODIS snow cover fraction data are not available for most winter cases, occurring in the dark seasons of the northern and southern hemispheres. Due to this limitation, we have not used the MODIS snow cover information in this study. Note that the percentage of data points characterized by a cold background surface (T_{2m} < 270 K) is 88%. This indicates that most of land pixels in the dataset are likely frozen or snow covered. Table 1 provides a list of all products available in the dataset built from coincident GMI/CloudSat observations (March 2014 - May 2016), and the main variables used specifically in this study.

In the original GMI-CPR dataset, CPR products are kept at their native resolution while the GPM data (e.g., GMI TBs), ECMWF auxiliary variables, and surface variables, are mapped to the CPR swath using a nearest neighbor approach. In this study (except for the case study analysis in Section 6.1), in order to have a one-to-one correspondence between the GPM and the CloudSat data, a mean CPR profile (and surface snowfall rate) is computed and associated to each GMI pixel (i.e., TB vector) along the CPR swath, by averaging all CPR profiles associated with the same GMI pixel. The final GMI-CPR global dataset consists of 529350 coincident pixels at GMI high-frequency channel resolution (~5 km), with 48194 snowfall coincident pixels. Figure 1 shows the global distribution of snowfall elements in the GMI-CPR coincidence dataset. Each snowfall occurrence is defined by the non-zero mean surface snowfall rate computed from the CPR 2C-SNOW V4 profiles associated with a GMI TB vector. The largest number of occurrences is found around 60°N and 60°S. It is worth noting that the highest latitude in the GMI/CPR dataset is 69°N/S.

This study investigates GMI high-frequency ΔTB signals in the presence of snowfall under different environmental conditions at higher latitudes benefiting from the high number of concurrent GPM and CloudSat overpasses in these regions. Ambient atmospheric water vapor content and cloud microphysical properties are also combined with surface information using a novel decision tree approach to quantify 166 GHZ TB responses over different surface types.

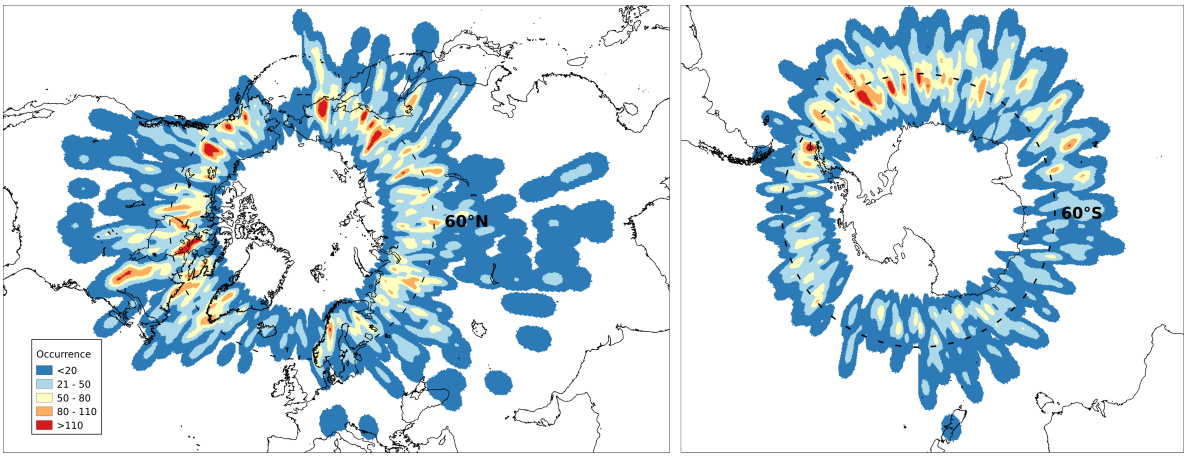

Figure 1. Global distribution of snowfall elements in the GMI-CPR coincidence dataset (March 2014 - May 2016). The two panels show the number of occurrences of snowfall elements (indicated by the colors) in the Northern (left) and Southern (right) hemisphere.

6. CloudSat-based assessment of GPM Microwave Imager snowfall observation capabilities

6.1 Case studies

Three main case studies that are part of the combined GMI-CPR snowfall dataset are analyzed. One describes an intense, widespread frontal snowfall event, the second an orographic snowfall event, and finally an extensive, deep synoptic snowfall case over the Labrador Sea. The original 2B-CSATGPM dataset is used for the case study analysis, with CPR products at their native resolution, and all other variables mapped to the CPR pixel positions along the swath. Therefore, replications of the same TB values associated with different, adjacent CPR pixels along the CPR orbital swath may be found.

6.1.2 Case 1: Intense snowfall event on 30 April 201

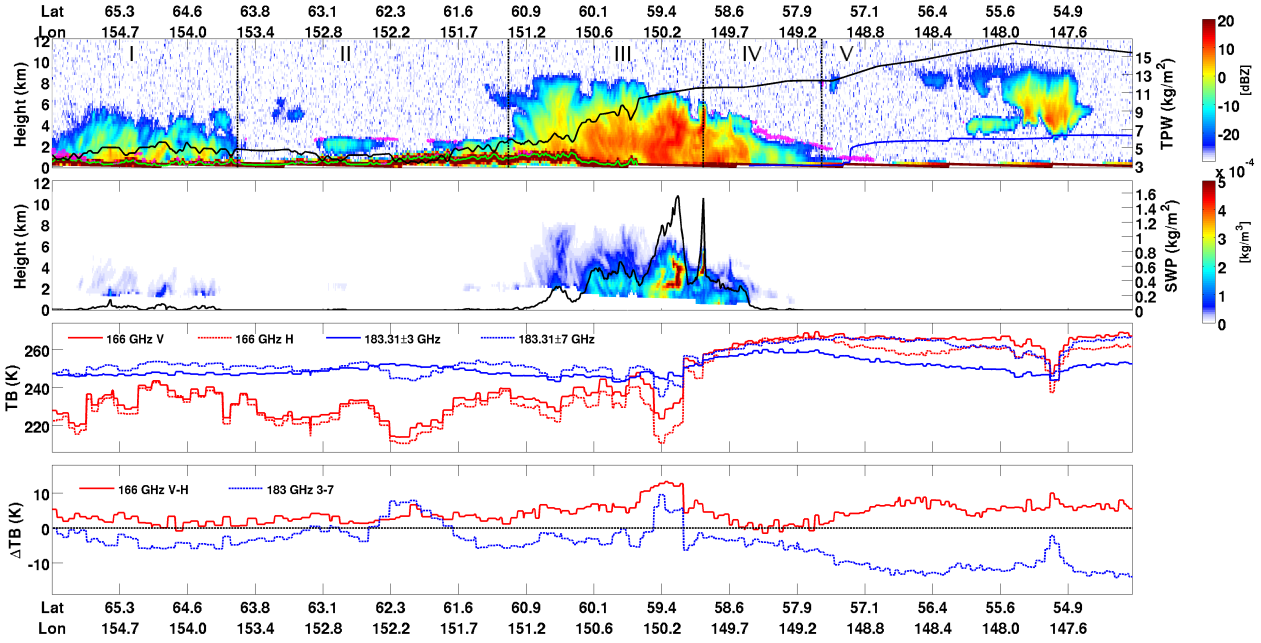

Figure 2a. Snowfall event on 30 April 2014. From top to bottom, the first panel shows height-lat/lon imagery of CPR reflectivity (colorbar, in dBZ), the freezing level height (blue curve), and TPW (black curve, with values provided on the right-hand side y-axis), along the CloudSat track. In this panel, cloud layers where the DARDAR product identifies supercooled droplets are superimposed and shown in magenta. Second panel shows height-lat/lon imagery of 2C-SNOW snow water content (SWC) (colorbar, in kg m^{-3}) and the snow water path (SWP) (black curve, with values provided on right-hand side y-axis). Third panel: GMI TBs closest to each CPR pixel along the CloudSat track at 166 GHz (V and H polarization, in red), 183.3±3 GHz and 183.3±7 GHz (in blue). Bottom panel shows GMI TB difference (ΔTB) at 166 GHz (V-H, in red), and for the two 183.3 GHz channels (in blue). In the top panel, vertical lines delineate different Sectors (I to V) identified in the discussion (see text for details).

This widespread frontal snowfall event in Eastern Russia on 30 April 2014 was first highlighted from a combined CPR and DPR perspective in Casella et al. (2017). Maximum cloud top heights reach ~8 km in the central portions of this CloudSat overpass segment, with lower snow-producing clouds located on the fringes of this snowfall event. A separate snowfall event with cloud top heights near ~ 5 km is also associated with surface snowfall in the far north and east segment of this overpass (Figure 2a top panel). The highest radar reflectivities are ~15 dBZ in the most intense central snowfall regions (Sector III), while reflectivites are much lower in both the shallow fringe central snowfall zones (Sector II) and the snowfall event located to the north and east (Sector I). SWC retrievals from the CloudSat 2C-SNOW product exceed $5x10^{-4}$ kg m^{-3} up the ~5 km level in the most intense precipitation cores, but SWC values do not exceed $2x10^{-4}$ kg m^{-3} in the other surface snowfall cloud structures. Near surface snowfall rates also exceed 2 mm h^{-1} in the most intense precipitation regions of this event. It is worth noting that, as evidenced in the second panel of Figure 2, 2C-SNOW SWC is available only above the first clutter-free bin which changes

depending on the background surface (higher for snow cover and sea ice, and lower over ocean). Therefore, CPR may miss the snowfall in the first 1000-1500 m above the surface (see also Milani et al., 2017). For example, for the weaker cloud north of 64°N (Sector I), the SWC is not available at the lower levels. This might lead to underestimations in the SWP and surface snowfall rate estimates. An elevated non-precipitating cloud structure is located to the south and west, with cloud top (base) values near 10 (5) km. Maximum reflectivities associated with this cloud approach 10 dBZ near the cloud base.

This particular case is interesting to analyze since it exhibits a land-to-ocean transition (59.6°N-150.3°E), with extremely dry TPW values near ~2 kg m^{-2} in the north sector of the scene increasing to over 15 kg m^{-2} in the southern sector (Figure 2a, top panel). A particularly significant TPW change is observed south of 59°N, indicating a distinct frontal structure evidenced also by the surface pressure field (not shown) (note the 183.3±3 GHz response to this TPW gradient). Land surfaces are very likely snow covered at this latitude.

In the deeper snowfall segments (Sector III), 166 GHz and 183±7 GHz TBs show some sensitivity to columnar ice content scattering effects that produce decreasing TBs (i.e., ~15-20 K decrease in 166 GHz TBs compared to surrounding regions). In this segment, the 166 ΔTB also show a polarization increase corresponding to the deeper and most intense clouds. This 166 ΔTB feature is correlated to the 183 GHz TB difference (183.3±3 GHz TB – 183.3±7 GHz TB, hereafter 183 ΔTB) increase.

In correspondence of the weaker or shallower snow clouds (Sector I and II, north of 60°N), 166 GHz TBs are higher than in the cloud-free regions, where the low TBs (between 210 K and 220 K) are due to the very low water vapor emission (TPW < 2 kg m^{-2}) over a radiatively cold (likely snow-covered) background. The relatively warmer TBs at 166 GHz in correspondence of the snowfall in these regions are also due to another important effect. TBs at 166 GHz typically decrease due to scattering by sufficient columnar ice content, but this case highlights the sensitivity of 166 GHz to supercooled cloud liquid water. The presence of supercooled water near cloud tops in these shallow clouds has been verified using the CloudSat CPR/CALIPSO DARDAR product as shown in Figure 2a (magenta color layers in the top panel). In the work by Liu and Seo (2013) similar TB increases was noted due to cloud liquid water that often mask frozen hydrometeor scattering effects and further complicate high microwave frequency TB signatures associated with snowfall events.

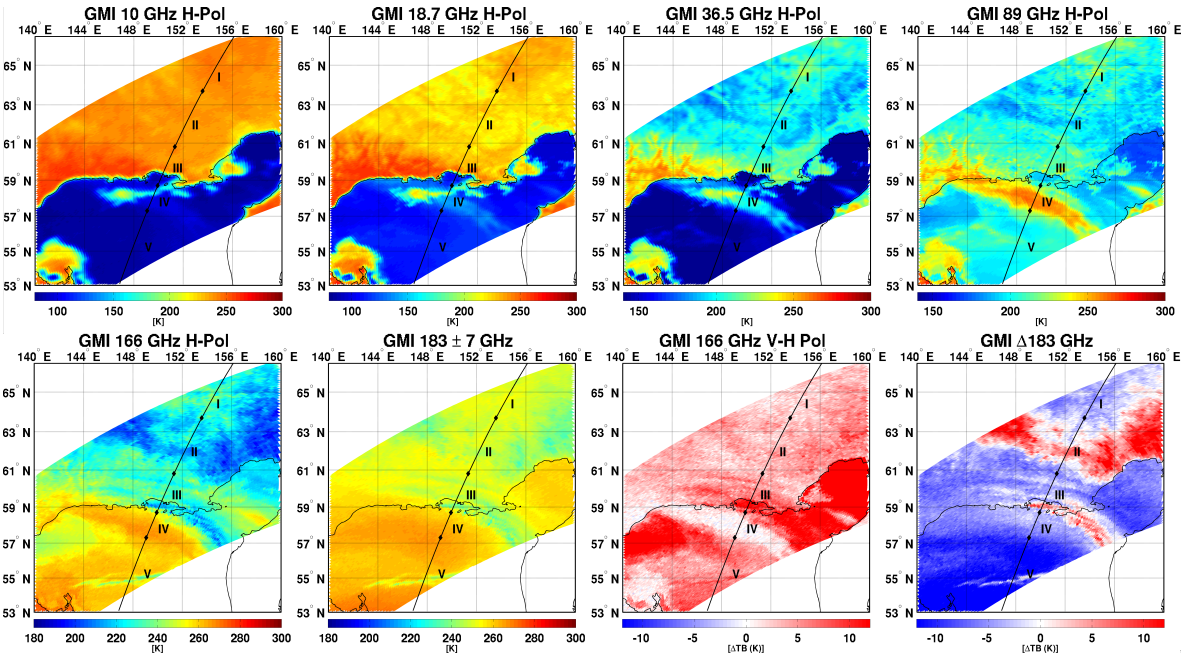

Figure 2b. GMI TB imagery corresponding to the snowfall event on 30 April 2014 shown in Figure 1. Top row from left, 10, 18.7, 36.5 , and 89 (H-pol) channels; bottom row from left: 166 (H-pol) and 183±8 channels, ΔTB at 166 GHz (V pol−H pol) and at 183.3 GHz (183.3±3 GHz – 183.3±7 GHz). The black line segment in each panel shows the CloudSat track. The sectors (I to V) identified in the discussion are also indicated (see text for details).

Moving south from 59°N (Sector IV and V), the 166 GHz and 183 GHz TBs progressively increase due to the atmospheric water vapor gradient. Atmospheric temperatures also increase further south (note the abrupt freezing level height increase around 57°N). This water vapor effect dampens the ice scattering effects due to the shallower and weaker portion of the clouds south of 58.6°N (Sector IV), where CPR shows lower reflectivity values (< 0 dBZ) and shallow surface snowfall structures (according the 2C-SNOW product). TBs at high frequencies (166 GHz and above) are not affected by such structures because of the water vapor dampening effect (where TPW > 10 kg m^{-2}), as the 166 GHz weighting functions peaks at higher levels with respect to the shallow clouds. The CloudSat CPR/CALIPSO DARDAR product indicates the presence of supercooled cloud liquid water droplets in the upper cloud layers (Sector IV, magenta layers). The effect of the emission by supercooled droplets is evident at 89 GHz (Figure 2b, top-right panel), while it is not visible at 166 GHz likely because of the stronger emission signal by the water vapor at this frequency. Moreover, 166 ΔTB approaches 0 K because of the depolarization effect of the cloud droplets. In this region (south of 58.6°N, and between 148°E and 152°E), Figure 2b shows faint warming signatures also at low frequencies (< 37 GHz) with respect to the radiatively cold oceanic surface background, thus indicating the presence of melting snow or drizzle at very low levels. At 10 GHz and 18.7 GHz frequencies, the emission signal is more evident west of 148°E, where it is very likely associated with predominantly liquid precipitation.

The high-frequency channels show sensitivity to the deep cloud with reflectivity exceeding 10 dBZ above 5 km (in Sector II), or in correspondence of the upper level cloud southward of 55.6°N (Sector V). It is also worth mentioning the significant 183 ΔTB (and to a less extent 166 ΔTB) signature associated with this cloud. This very distinctive feature highlights another issue – ΔTB may not be always linked to surface precipitation: at 183.3 GHz, the cloud may be optically thick from an ice extinction/scattering perspective, yet not deep enough to significantly affect 183±3 GHz TBs. At 166 GHz, non-precipitating ice clouds with reflectivity around 5-10 dBZ peaking at high levels (relative to the weighting function), may show significant polarization.

6.1.2 Case 2: Orographic precipitation event on 14 December 2014

A coastal orographic snowfall event near and over Alaska, USA is the main feature of this scene, with a transition from oceanic to land background (Figure 3). Extremely light and shallow rain and periodic overlying mid-level clouds with a freezing level near 1.5 km appear south of 60°N/146.9°W (Sector I, left-end side). A more intense and deeper (~ 5 km cloud top) rain core is located just north of 60°N/146.9°W (Sector I, right-end side), then the freezing level steadily declines. The surface rain/snow transition occurs near 61°N/147.6°W, coincident with the ocean to land surface transition (Sector II). Here coastal and orographic snow with embedded intense snowfall is located near 61.4°N/147.9°W. The estimated surface 2C-SNOW snowfall rates approach 5 mm h^{-1} in these embedded snow cores. SWC around $3x10^{-4}$ kg m^{-3} are located in the lowest portion of the coastal snow, while SWC exceeds $5x10^{-4}$ kg m^{-3} in the most intense snow core over mountainous terrain. Possible shallow and light surface snow exist over the mountains between 62.8°N/149.0°W and 64.2°N/150.1°W (Sector III). Elevated clouds not associated with surface snow above this mountainous shallow snow event are found to north and west through ~65.0°N/150.0°W (Sector IV). Reflectivities are generally low, although cloud structure thickness is ~4-5 km, with cloud base (top) near 3-4 (8-9) km. Another shallow, mostly light, snowfall layer over land is also located in the far northwest portion of this scene (Sector V). The most intense reflectivities are generally under 10 dBZ located near 66.9°N/152.7°W, and SWC and surface snowfall rates are accordingly low.

TPW values vary widely over this scene. The TPW is relative stable over the ocean (~11-12 kg m^{-2}), decreases sharply over the mountainous terrain (~4-7 kg m^{-2}), increases again to near 9 kg m^{-2} over lower land surfaces near 64.2°N/150.1°W, then steadily decreases to near 5 kg m^{-2} in the far north and west portions of the scene. Unlike the first case study that showed a drastic TPW change corresponding to tangible 183.3±3 TB changes, the 183.3±3 GHz TBs associated with this case exhibit relatively subtle changes despite the varying TPW, with warmer TBs over ocean than over the mountain and land surfaces. The 183 ΔTB quickly transitions to a positive value immediately to the north and west of the most intense precipitation over the highest terrain in the center of the scene (~60.7°N/147.6°W), where TPW values are extremely low.

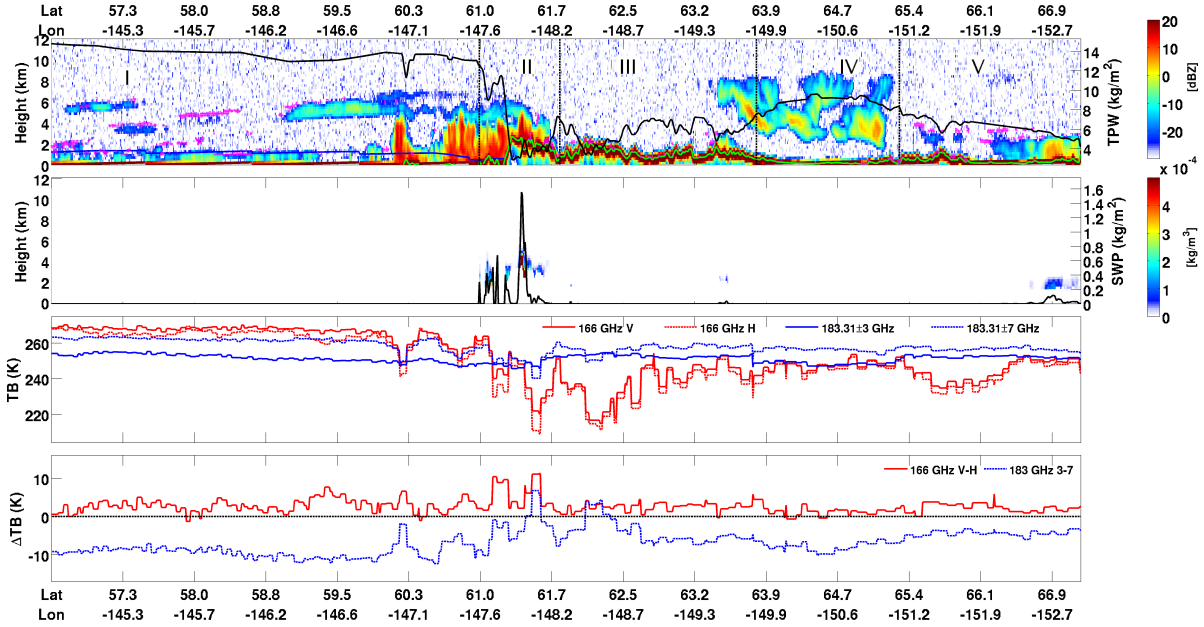

Figure 3. Same as in Figure 2a but for orographic event on 14 December 2014.

The 166 GHz and 183.3±7 GHz channels also exhibit interesting and varying sensitivity to the precipitation structures in this scene. Over the ocean (Sector I), 166 GHz TB are quite warm (~270 K) with 166 ΔTB values between 0-5 K. The shallow rainfall laden with cloud and rain liquid droplets greatly increases atmospheric opacity and virtually eliminates 166 GHz polarization differences that would be expected over the highly polarized ocean surface under clear skies. The 183.3±7 GHz channel is insensitive to these shallow rain structures due to sufficient lower atmospheric opacity attributed to water vapor.

Two deeper rain structures located further to the north and west (Sector I, right-end side) again illustrate the sensitivity of high-frequency, scattering sensitive GMI channels to columnar ice. The deepest rain cloud near 59.4°N/146.6°W induces a ~30 (20) K 166 (183.3±7) GHz TB reduction due to scattering by ice particles above the freezing level. 166 ΔTB values also slightly increase due to this precipitation feature. 183 ΔTB values, however, respond vigorously. The 183 ΔTB is an extremely valuable metric for some precipitation events due to the lack of 183.3±3 GHz sensitivity to columnar ice in systems that are deep enough to affect 183.3±7 GHz TB's, but with cloud tops low enough to allow sufficient water vapor absorption/emission to effectively render 183.3±3 GHz measurements invariable. The second deep rain core near 60°N/146.9°W reaches as high, or slightly higher, than the previous rain feature, but reflectivity magnitudes are slightly lower. Both 166 GHz and 183.3±7 GHz TB depressions are accordingly not as low – about 15-20 K for both channels. A 183 ΔTB signature also accompanies this feature, albeit with a smaller magnitude than the other rain feature.

The coastal and orographic snowfall (Sector II) shows interesting, yet different, 166 GHz responses compared to the deeper oceanic rain profiles. TBs at 166 and 183.3±7 GHz both decrease in the deeper and most intense snowing cloud structures due to snow/ice scattering effects. 166 GHz TBs show enhanced sensitivity and a much larger TB decrease (~20-30 K) compared to the 183.3±7 GHz TBs near the intense upslope snowfall located near 60.4°N/147.2°W. The intense upslope snow also corresponds to a noticeable polarized signal, with 166 ΔTB values near 10 K despite being located over an unpolarized land surface. This 166 GHz polarized signal is presumably also due to ice scattering effects (e.g., Gong and Wu, 2017). Note that 166 GHz TB reductions are not as strong, however, just to the northwest in the snowfall core located at the highest elevations near 60.7°N/147.6°W despite SWP retrievals indicating the highest ice content in this region. Maximum SWP estimates exceed 1.5 kg m^{-2} in this zone, compared to under 0.6 kg m^{-2} in the most intense upslope snow located to the south and east. Surface emissions at the highest elevations under low TPW conditions strongly affects the 166 GHz signal, much more than the 183.3±7 GHz signal.

Moving further to the north and west, the 166 GHz channel displays a warming response to the very shallow snowfall event over higher terrain near 62.8°N/149.0°W (Sector III, right-end side). 183 GHz TBs are unaffected by this shallow precipitation feature. The non-precipitating mid-level clouds further to north and west (Sector IV) show some 166 GHz TB reductions due to either ice scattering and/or surface emissivity effects, embedded in the significantly higher mean TB values (20 K) with respect to the adjacent clear sky regions [probably due to the higher TPW found in correspondence of these mid-level clouds, as confirmed by the very low 166 ΔTB (ΔTB ~ 0 K)]. It is worth noticing also, that there is an interesting sudden and concurrent decrease in 166 (~10 K) and both 183 GHz channel TBs (~ 5 K) near 63.0°N/149.2°W that corresponds to an increasing TPW zone and the elevated CPR reflectivities located at ~6 km altitude. This feature is probably related to scattering at all frequencies since sufficient ice content is located at high altitudes with low enough ambient water vapor values to cause a 183.3±3 GHz weighting function downward shift that makes it sensitive to ice. Note that the 183 ΔTB values are stable in this zone, thus illustrating unison in the respective 183 GHz channel responses.

The final noteworthy precipitation feature is the shallow snow-producing cloud structure near 66°N/152°W (Sector V). The 166 GHz TBs increase of about 25 K in correspondence with these shallow clouds compared to the clear sky region located near 65.5°N/151.3°W. This response is again due to the supercooled droplets emission as confirmed by the CloudSat DARDAR product (shown as magenta color cloud layers in the top panel) and is confirmed by the absence of a polarization signal related to this shallow cloud, as opposed to a slight polarization observed with the snow-covered background under clear skies. This again confirms previous studies (e.g., Kneifel et al., 2010, Xie et al., 2012) showing TB and ΔTB enhancement at 150 GHz in presence of snowfall, while damping of the polarization signal was obserevd in the presence of supercooled water. This also confirms the finding by Liu and Seo (2013) that describes an emission signal at high frequencies in the winter associated with snowfall in the presence of a frozen surface background (low moisture and cold conditions). This effect was not visible at 166 GHz for the 30 April 2014 case study previously described because of the high TPW.

6.1.3 Case 3: Synoptic snowfall event over the Labrador Sea 27 March 2014

Figure 4a shows an extensive, deep synoptic snowfall case over the Labrador Sea between Greenland and the Canadian maritime provinces, with an open water/sea-ice transition around 61°N-58°W. This snowfall event occurred in a cold, dry environment (TPW < 10 kg m^{-2}) over the whole region, becoming extremely dry (TPW < 5 kg m^{-2}) over the sea ice formations (north of 60.5°N). CPR shows a 6-8 km deep cloud with peaks of reflectivity around 10-15 dBZ, associated with a SWP reaching 1.6 kg m^{-2} in correspondence of the deepest cloud (Sector I). Peak SWP values are associated with particularly high SWC located above 6 km southward of 57.5°N. Shallow snowfall structures also appear as a distinctive separate cloud structure northward of about 59.8°N-57.2°W, although embedded shallow convective structures are also evident in the lowest ~1 km as far south as about 58.4°N (Sector II).

The 166 ΔTB is around 10-15K in the most intense portion of the cloud over ocean. It increases gradually as the cloud gets less intense, and as TPW decreases, because of the increasing surface emission contribution to the signal, exceeding 20 K between 59.6°N and 61°N (Sector III). Here CPR evidences the presence of a multilayer cloud, with a shallow cloud layer (< 1 km thick), and a higher level cloud with maximum reflectivity around 0 dBZ. The spotty snowfall retrieval in this sector, particularly evident around 60°N is due to the weak reflectivity signal at the lower bins, and to the fact that 2C-SNOW product provides SWC profile only if Z at the first clutter free bin is higher than -15 dBZ. The increase of ΔTB in this region is due to a combination of effects: the effect of the sea surface, the possible existence of mixed-phase clouds containing supercooled water, and the polarization effect induced by the ice crystals in the upper level cloud. As a matter of fact, 166 ΔTB starts decreasing north of 61°N (Sector IV), where an upper level cloud exists that is not associated with precipitation, but sea ice is present at the surface [as evidenced by the GMI TB maps at frequencies below 89 GHz in Figure 4b, and confirmed by the sea ice concentration map (not shown)]. This shows that the upper level cloud alone does not explain the high 166 ΔTB observed over the open water region, which is mostly due to the surface. In the cloud free regions, the mean ΔTB values in presence of sea ice is below 10 K (lower than the values over ocean in presence of intense snowfall as evidenced also in Figure 4b), and both TBs and 166 ΔTB show a large variability. It is worth noting the large

range of variability of TBs at 166 GHz (both V-pol and H-pol) for this event compared to the 183.3 GHz channels, with values ranging between 205 K (for the deepest cloud) to 220 K (for the multilayer cloud) for 166 GHz H-pol and between 220 K (for the deepest cloud) and 245 K (for the multilayer cloud) for 166 GHz V-pol, with TB for H-pol always lower than V-pol as evidenced also by Gong and Wu (2017) 183 ΔTB shows positive values up to about 10 K in correspondence of the deeper and most intense snowfall (Sector I, see also bottom right panel in Figure 4b) and negative values elsewhere. However, it shows values and variability similar to the clear sky region over sea ice (Sector IV), where all TBs below 37 GHz show large variability related to sea-ice concentration.

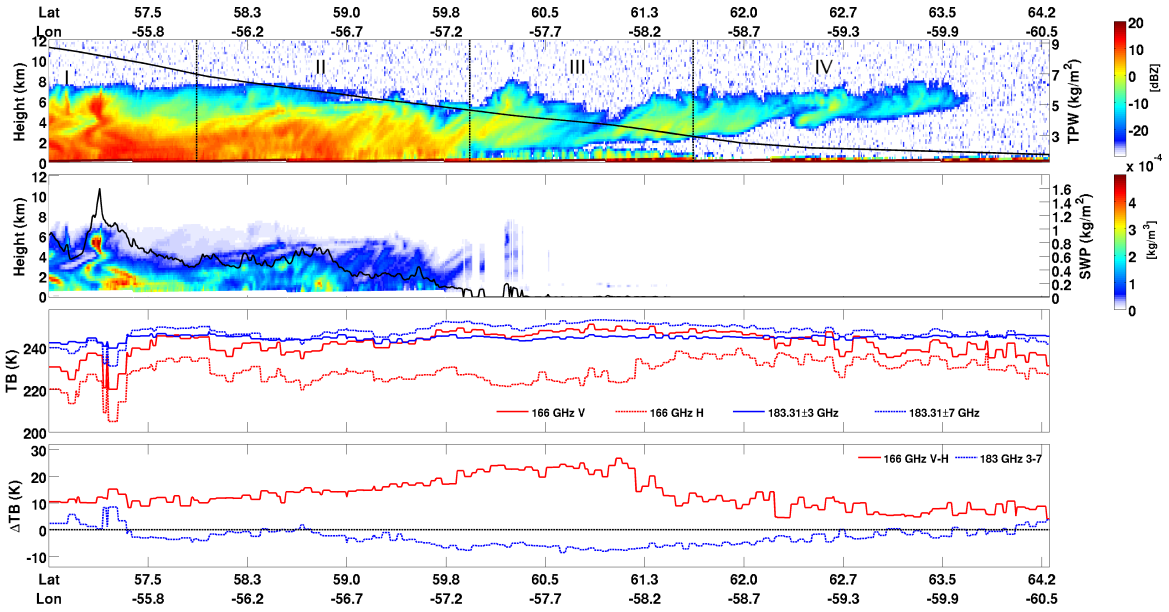

Figure 4a. Same as in Figure 2a but for synoptic snowfall event over the Labrador Sea on 27 March 2014

Figure 4b. Same as Figure 2b but for the synoptic snowfall event over the Labrador Sea on 27 March 2014

This case study shows that the proper characterization of the state of the sea surface at higher latitudes, especially in dry conditions (TPW < 10 kg m^{-2}) is necessary to be able to correctly interpret the GMI signal at high frequencies and relate it to snowfall: on one side, low frequency channels can be effectively use to delineate regions of sea ice and different sea-ice concentration, as shown in the top panels of Figure 4b, with large variability over the sea ice and no signal related to the cloud even in correspondence of the snowfall region; on the other side the use of the high-frequency channels, and in particular the use of 166 and 183 ΔTBs, can provided the information needed to correctly interpret the signal related to snowfall (see bottom panels in Figure 4b).

The three case studies illustrate the complicated and multi-faceted TB signatures associated with different snowfall modes (e.g., deep versus shallow snow layers) and cloud microphysical composition under different ambient atmospheric conditions over varying surfaces. They also illustrate the value of high-frequency GMI channels to elicit new ways of exploring such events.

6.2 Analysis of the GMI channel capabilities for snowfall detection

In order to define some general, more quantitative criteria on the use of GMI 166 GHz channels, and in particular the polarization signal at 166 GHz (166 ΔTB), for snowfall detection, a global GMI-CPR dataset analysis is carried out in this section. It is worth noting that GMI is the first spaceborne radiometer equipped with high frequency (> 100 GHz) dual-polarization channels and, while numerous previous studies have thoroughly studied 183 GHz channels for surface snowfall application few studies have analyzed high frequency channel polarization sensitivity to snowfall, and these are based on ground-based measurements.

In this analysis all the variables associated with CPR profiles (e.g., SWC, SWP, surface snowfall rate, TPW) are averaged to obtain a one-to-one correspondence between GMI TBs and CPR variables and without altering GMI observations, therefore the values shown in this section are different from those shown in the case studies analysis, where they were at the native CPR spatial resolution. The analysis is carried out considering as snow events pixels where the averaged CPR 2C-SNOW surface snowfall rate higher than 0 mm h^{-1}.

In order to investigate GMI sensitivity to snowfall, we focus on the 166 GHz channel, and analyze the relationship between ΔTB and TBs at 166 GHz in relation to the environmental conditions (surface type, and TPW), and snowfall amount (SWP). It is worth noting that, as opposed to Gong and Wu (2017), the analysis focuses mostly on higher latitudes (around 60°N/S) because it is carried out only for snowfall pixels in the GMI-CPR coincident datasets (see Figure 1). The 2C-SNOW SWP was used to identify snowfall profiles. Such identification is subject to the limitation of the 2C-SNOW product: on one side, the snowfall manifold, made of profiles where SWP > 0 kg m^{-2} (i.e., containing snow at the surface according to 2C-SNOW product), may have SWP underestimated (i.e., because snowfall below the first clutter-free bin level is missed in the 2C-SNOW product). One the other hand, it might exclude snowfall profiles with a weak signal (Z at the first clutter-free bin level below -15 dBZ), or shallow snowfall events, for which 2C-SNOW SWP = 0 kg m^{-2}.

Figure 5 shows the distribution and occurrences (2-D histogram) of the snowfall pixels of the whole GMI-CPR dataset in the 166 GHz ΔTB/TB 2-D space (divided into 200x100 bins). Each dot represents the mean ΔTB and TB values in each bin while the colorbar indicates the % of occurrences. Contours identifying the 90% of occurrences in the snowfall manifolds associated with the different background surfaces identified by the tree analysis (land, open water, sea ice) are also shown. The SIC concentration SIC > 57% has been used to separate sea ice from open water. While 166 ΔTBs are positive, as in Gong and Wu (2017) the distinctive bell-shaped ΔTB curve as a function of V-pol TB (peaking near 10 K) is not found. The minimum TBs are rarely found below 200K because of the weak scattering effect by the ice particles associated with snowfall at higher latitudes. Moreover, the behavior of 166 ΔTB versus TB in the upper right portion of the scatterplot (for the whole and open water manifolds) corresponds to what is shown in Gong and Wu (2017) at 89 GHz. The highly polarized signal (high 166 ΔTB values) is due to the large impact of the background surface and to the low opacity of the atmosphere in dry conditions. There is a very distinct behavior of the ΔTB/TB relation for the three different surface types. It is worth noting the different shape and range of 166 ΔTB values of the sea ice manifold with respect to the open water manifold, and its

similarity to the land manifold due to the lower polarization found in both cases with respect to open water. The range of TB values at 166 GHz (V-pol, but the same holds for H-pol) for the three manifolds, however, is quite different.

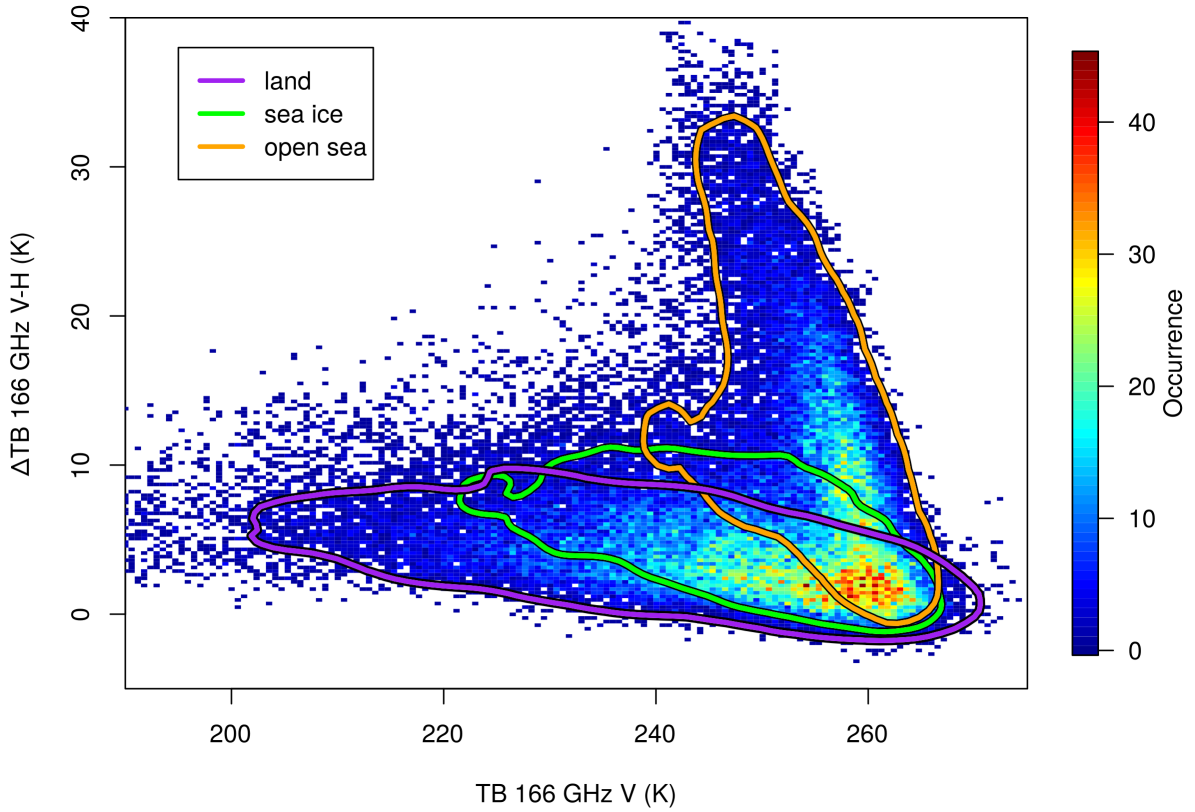

Figure 5. Scatterplot of the 166 GHz ΔTB/TB 2-D histograms for the whole GMI-CPR snowfall dataset. The 2-D histogram is created by dividing the ΔTB/TB space in 200x100 bins. Each dot represents the mean ΔTB or TB value in each 2D bin while the colorbar indicates the % of occurrences. Contours for 90% occurrences in the three background surface manifolds are also superimposed: open water (orange), land (purple), sea ice (SIC > 57%) (green).

Figure 6 shows the same distribution of the snowfall pixels as Figure 5 in the ΔTB/TB 2-D space with mean SWP and TPW values for each bin indicated by the colorbars. The results are shown for land (with T_{2m} < 270 K for 88% of pixels), open water (SIC<57%), and sea ice (SIC > 57%). Over land we observe that for TPW > 3-4 kg m^{-2}, for any given TB value, ΔTB increases as the SWP increases, showing a good correlation between 166 ΔTB and snowfall. These results show that ΔTB can be a valuable parameter for snowfall detection over land when the atmosphere is moist enough to mask the signal from the radiatively cold background (i.e., TPW > 3.5 kg m^{-2}). For lower values of TPW, there is no evidence of a relationship between ΔTB or TB with the SWP. The same holds for 166 GHz TB (V-pol) > 260K. In this region of the scatter diagram where the bins are characterized by large TPW (TPW > 10 kg m^{-2}) and low SWP values (SWP < 0.01 kg m^{-2}), the water vapor dampens the polarization effect at 166 GHz, while its emission reduces the weak scattering effect due to the snow. It is also worth noticing that the largest snowfall amounts (SWP > 0.5 kg m^{-2}) are mostly found for 220 K < TB < 260 K.

Over ocean (open water or SIC < 57%) two different regions can be identified. Depending on the snowfall regime the behavior of ΔTB versus TB changes significantly. One region is characterized by a linear relationship between ΔTB and TB for the lower SWP values (SWP < 0.1 kg m^{-2}), with decreasing ΔTB (from 30 K to 0 K), and increasing TB (from 260 K to 270 K) as TPW increases, as expected, and with a slight dependence on SWP. In this region, the ΔTB signal is either dominated by the surface contribution or by the dampening effect on the TB polarization by the water vapor. The other region is characterized by the largest values of SWP (SWP > 0.1 kg m^{-2}) associated with high values of TPW, but also in this case the impact of snowfall on the TB polarization is not significant. Over open water ΔTB is not related to snowfall due to the high polarization induced by the surface. On the other hand, 166 GHz TBs are more correlated with SWP, as the lowest TBs are associated with the highest SWP. Therefore, over open water (or low SIC),

TBs at 166 GHz could be used to retrieve snowfall intensity, mostly in presence of intense snowfall events and moist conditions (SWP > 0.5 kg m^{-2}, and TPW > 10 kg m^{-2} as evidenced in Figure 6).

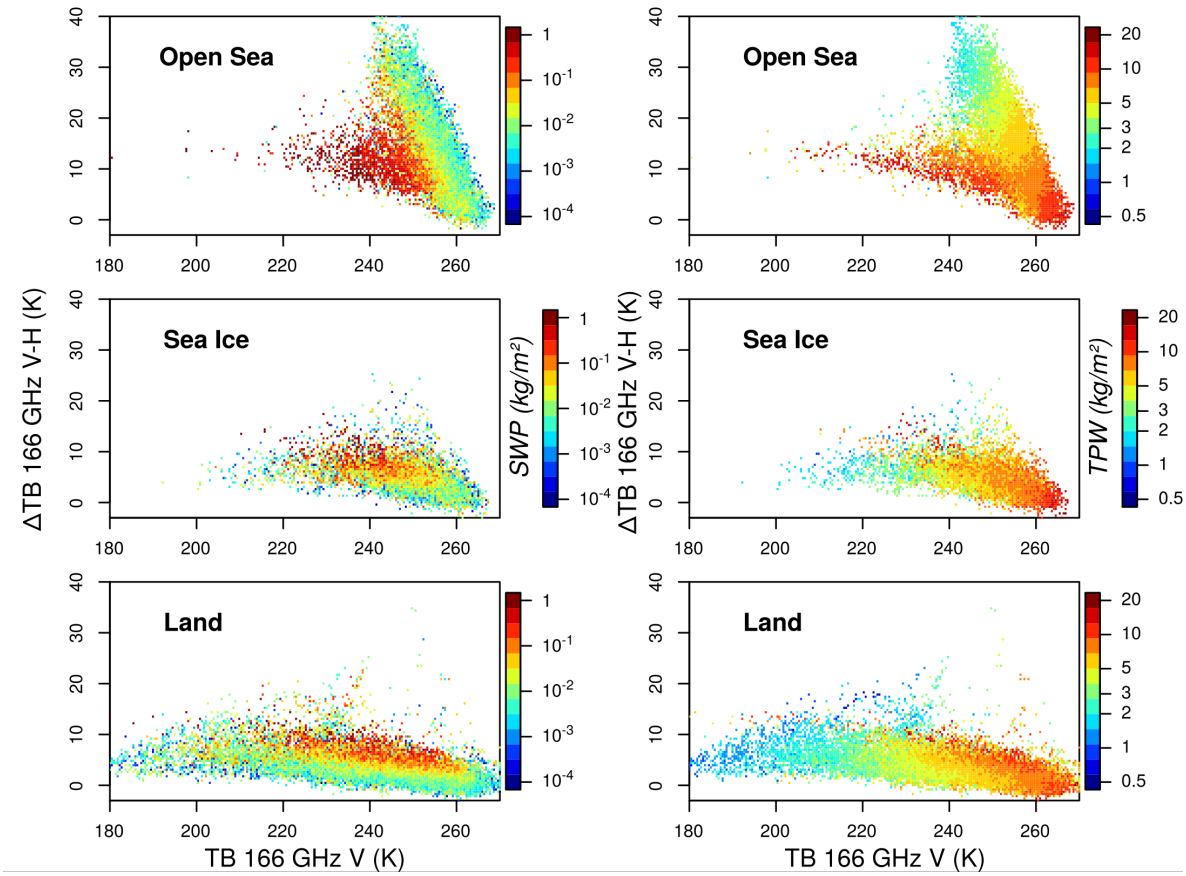

Figure 6. Scatterplots of the ΔTB/TB for snowfall pixels in the three surface type manifolds: open sea (SIC < 57 %) (top), sea ice (SIC > 57%) (middle row), and land (bottom row). ΔTB/TB space is divided into 200x100 bins, and the mean SWP (left panels) and TPW (right panel) values in each ΔTB and TB bin are represented (in log scale).

Over sea ice, the almost linear relationship found between ΔTB and TB is similar to the land signature because of the lower impact on the polarization due to the water surface. The ΔTB signal is also strongly related to the SWP (decreasing as the SWP increases). TPW has a lower range of values with respect to open water, with TPW mostly < 5 kg m^{-2}. These results show that 166 ΔTB can be a useful variable for snowfall detection (and retrieval) over sea ice, as well as over land. As SWP increases, 166 ΔTB increases when the TPW is above a given threshold (lower over land than over sea ice) (4 kg m^{-2}). However, while over land TPW has a much larger range of variability and TBs at 166 GHz (ranging from 170 K to 270 K) do not show a strong relationship with SWP, over sea ice TPW variability is lower, and the TBs show a stronger dependence on SWP, decreasing from 270 K to around 220 K as SWP increases.

6.3 Impact of supercooled droplets on GMI snowfall signal

In Section 6.1 we highlighted the significant impact that a supercooled water layer can have on TBs and ΔTB at 166 GHz. We have also evidenced that such an impact is strongly dependent on the environmental conditions. In order to analyze further the sensitivity of the GMI 166 GHz channels to snowfall, and to illustrate the impact of supercooled droplets on the signal, we have compared the behavior of both ΔTB and TB in clear sky to that in presence of snowfall, and in presence of snowfall and supercooled droplets (embedded in the cloud, or at the top layers of the cloud, which occurred in 72% of snowfall cases) as inferred from the CloudSat DARDAR product. The whole GMI-CPR dataset has been divided into four sub-groups: clear sky (CS, which means SWP = 0 kg m^{-2}), snowfall (SN, for SWP > 0 kg m^{-2}, and no supercooled water), snow with supercooled droplets on the top cloud layers (SCT), and snow with supercooled droplets embedded in the cloud (SCE). It is worth noting that the radar-lidar combination in

the DARDAR product is very useful for distinguishing cloud phase. While the lidar is able to identify accurately the presence of a supercooled layer on top of the cloud, the embedded supercooled droplets identification is less certain as it might be missed in some cases (J. Delanoë, personal communication). Therefore, the snowfall manifold (SN) might actually include cloud profiles with supercooled droplets embedded in the cloud. Moreover, the clear-sky (CS) manifold might include shallow or weak snowfall cases (with or without supercooled droplets) missed by the 2C-SNOW product (as evidenced in the case study analysis in Section 6.1). However, we have verified that it is meaningful to analyze the behavior of the GMI 166 GHz channels to snowfall considering these different manifolds (SN, SCT, SCE, and CS) by testing that the distributions of 166 ΔTB and TB for each pair of manifolds are statistically different from each other.

Each sub-group has been categorized in bins according to TPW (dividing the TPW range in 21 bins) and according to SWP (dividing the SWP range in 11 bins). Then, for each subgroup and for each bin, the median 166 ΔTB and TB values have been computed. Figures 8 and 9 show the median values found in each bin (TB V-Pol in Figure 7, and ΔTB in Figure 8), as a function of the TPW (top panels) and SWP (bottom panels). The results are shown for land and sea ice, the conditions where 166 ΔTB responds mostly to the cloud and is less contaminated by the surface.

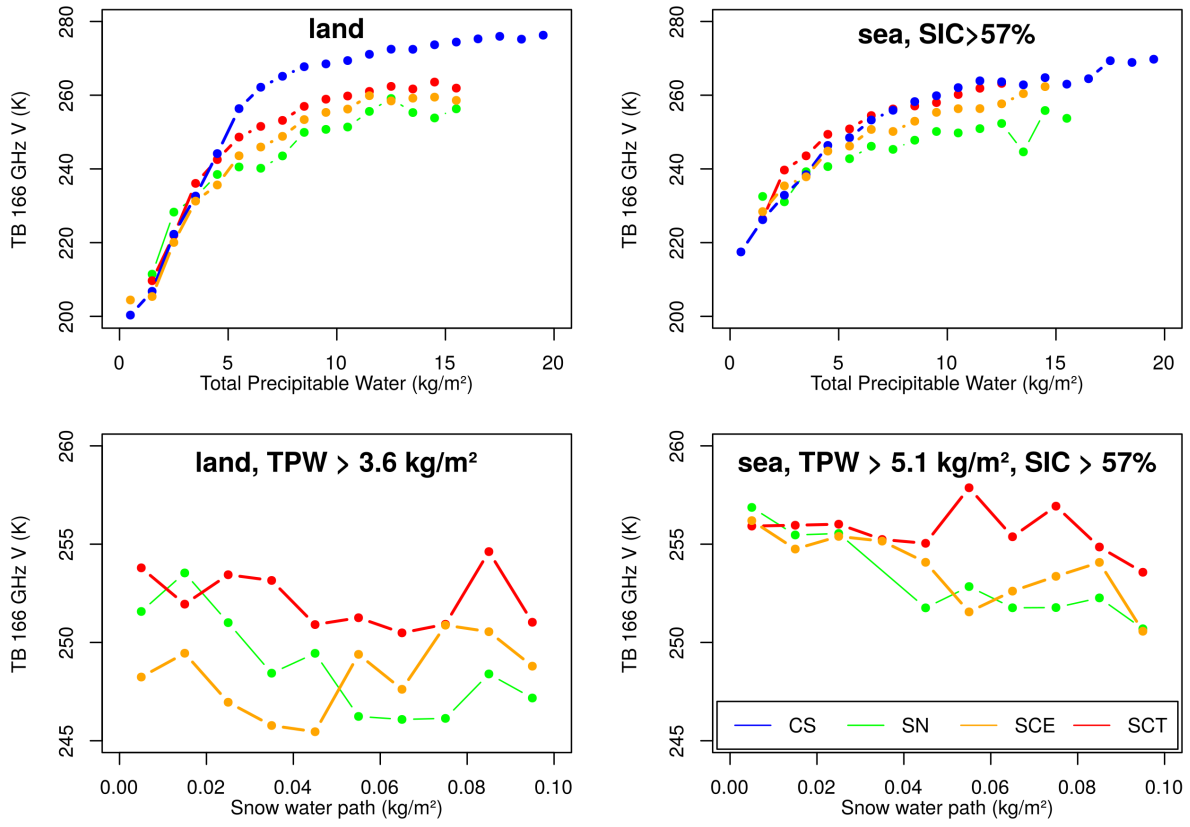

Figure 7. Median values of TBs at 166 GHz (V-Pol) (computed in TPW and SWP bins) as functions of TPW (top panels) and SWP (bottom panels) for clear sky (CS, blue), snow (SN, green), snow + embedded layer of supercooled (SCE, orange), snow+ supercooled layer on top (SCT, red). The dataset has been divided into 21 TPW bins (top panels) and 11 SWP bins (bottom panels), and only the results for bins with at least 20 pixels are shown (for statistical significance).

In Figure 7, over land, mean TBs increase with TPW (as expected because of the increasing emission by the water vapor), and in presence of snowfall, and for TPW > 4 kg m^{-2}, the mean TBs of snowfall cases (SN) are systematically lower compared to clear sky (because of the scattering by the ice). However, the presence of supercooled droplets significantly impacts the TBs, especially when they are found on the top of ice cloud layers (SCT). In such cases, mean TBs can be up to 10 K higher (on average) than snow-only cases. This is due to the emission by the water droplets and also to the fact that, on average for each TPW bin, the SWP found in presence of supercooled droplets (SCT and SCE) is lower than for snowfall clouds

with no supercooled droplets (SN) [on the whole dataset SWP mean values are 0.04 kg m^{-2} for SCT, 0.10 kg m^{-2} for SCE, and 0.21 kg m^{-2} for SN]. Looking at the mean TB behavior as a function of SWP (Figure 7, bottom-left panel), it is evident that there is a decrease of TBs for snowfall cases (SN) as SWP increases and exceeds 0.03 kg m^{-2}. The effect of the supercooled droplets, however, is very significant, and it attenuates the ice scattering effect (shown for SN by the TBs decreasing as SWP increases), especially when droplets are found on the top of the ice cloud layer (SCT). When the supercooled droplets are embedded in the cloud (SCE) the effect is less clear, median TBs appear lower than snow-only cases for SWP < 0.04-0.05 kg m^{-2} and higher for larger SWP values. It is worth noting that in presence of supercooled droplets over land (both SCT and STE), 166 GHz TBs do not show a significant trend with the SWP because the cloud droplet emission compensates for the scattering effects by the ice cloud.

Over sea ice (SIC > 57%), a clear distinction of the median 166 GHz TBs versus TPW curves in clear sky (CS) and with snowfall (SN) is visible only for TPW > 4 kg m^{-2}, with median TBs lower for SN than for CS (Figure 7, top-right panel). In such conditions, the effect of the supercooled droplets is to significantly increase the TBs up to values comparable to CS when they are on top of the ice cloud layer (SCT), and to values between CS and SN when they are embedded in the cloud. In very dry conditions (TPW < 5 kg m^{-2}), the supercooled droplet emission effect on TBs is noticeable. When they are on top of the cloud layer (SCT), TBs are higher than for CS or for SN. When the supercooled droplets are embedded in the cloud (SCE), the effect of the emission by the droplets is reduced, and median TBs become comparable to CS (or to SN). It is worth noting that over land (top left panel), in very dry conditions, all curves almost overlap to each other, showing no effect of the presence of supercooled droplets on the median TBs. However, the effects of supercooled droplets on the TBs were highlighted in the case study analysis (Section 6.1.2). In very cold and dry conditions (i.e., and when the emission by the water vapor at 166 GHz is negligible) [e.g., northern portion of the Frontal snowfall case (Section 6.1.1), and Orographic Case (Section 3.1.2)] supercooled droplets on top of the ice cloud layer corresponded to 166 GHz TB increases in presence of snowfall with respect to the clear sky region. We also noticed that in moister conditions such effects are masked by the water vapor emission (southern portion of the Frontal snowfall system, Section 6.1.1). In both cases the background surface was land (very likely snow covered).

The effect of supercooled droplets is also evident in the bottom-right panel (sea ice). Here we note a trend of the TBs with the SWP (TBs decrease as SWP increase) for SWP < 0.04-0.05 kg m^{-2}, while for larger amounts of snowfall such a trend is not evident (analogously to what was found over land). In presence of supercooloed droplets, median TBs are found comparable to snowfall-only cases (SN) when they are embedded in the cloud (SCE) and for any value of SWP. When they are on top of the ice cloud layer (SCT), and for SWP > 0.04-0.05 kg m^{-2}, the effect is to reduce the scattering effect on the TBs, and the associated TBs are up to 8-10 K (on average) higher compared to SN. These results show that also over sea ice the use of TBs at 166 GHz for snowfall detection can be quite problematic in presence of supercooled water droplets.

Note that the significance of the results shown in Fig. 8 (i.e., presence or absence of trends) has been tested by carrying out a statistical test on the Spearman correlation coefficient for each pair of variables (TB vs. SWP, and TB vs. TPW) in each manifold (for the ranges shown in Fig. 8). The test confirmed that all trends shown over land and sea ice in Fig. 8 by the median values are significant and represent the trends between the two variables in each manifold, except for SCE over land, and for SCT over land and sea ice (i.e., no trend was evidenced in these cases, as shown in Fig. 8).

In Figure 8 the behavior of 166 ΔTB for the different sub-groups is analyzed. Over land (top-left panel), for TPW < 4-5 kg m^{-2} it is evident the polarization by the surface in clear sky (CS). For TPW > 4-5 kg m^{-2}, SN shows higher ΔTB values than in clear sky (CS) due to the polarization effect by the ice at 166 GHz (see also Gong and Wu, 2017). In presence of supercooled droplets such effects are reduced, as the emission effect decreases the ice polarization effect. ΔTB median values are correspondingly lower compared to SN, and become comparable to clear-sky conditions when the droplets are found on top of the ice cloud. As pointed out above, this is also due to the fact that for each TPW bin SCT cases (and to a less extent SCE cases) are associated with SWP lower than for SN cases. It is very interesting to note that, as opposed to the TBs (Figure 8), ΔTB shows a very distinct trend in presence of snowfall, with ΔTB increasing as SWP increases (for SWP > 0.02 kg m^{-2}) (median values increasing from 1.5 K to 3 K as SWP increases). It is worth noting that these median values (e.g., ranging between 1.62÷3.18 K for SN, 2.04÷2.96 K for SCE, and 1.48÷2.91 K

for SCT over land) are much lower than what can be found for single snowfall events (e.g., ranging between -2.78÷28.83 K for SN, -2.49÷15.49 K for SCE, -3.28÷21.76 K for SCT over land). This was also evidenced in the case study analysis (Section 6.1), where, in the presence of snowfall, ΔTB could be as high as 10-15 K. In presence of supercooled droplets such trends are still visible (Figure 8, lower-left panel), and the behavior is similar when they are on top of the ice cloud or embedded in the cloud (SCT and SCE), as opposed to what is shown for 166 GHz TBs (Figure 8). These results show that the depolarization effect at 166 GHz induced by the cloud droplets is on average not enough to eliminate completely the polarization effect at 166 GHz by the ice crystals in presence of snowfall. This shows that ΔTB can be a very valuable parameter to use for snowfall detection and quantification for the following difficult circumstances: (1) over land, (2) for very weak snowfall events (very low SWP), and (3) for low TPW values in 4-5 kg m^{-2} range. Over sea ice (SIC > 57%), a similar ΔTB vs. TPW behavior exists (Figure 8, top-right panel) to what was found over land for TPW > 5 kg m^{-2}. SCT shows always lower 166 ΔTB than for CS, meaning that the presence of supercooled water droplets on top of the cloud attenuates the polarization signal by the surface also for very low TPW. However, the positive trend of ΔTB with SWP (Figure 8, bottom-right panel) is evident only for SWP < 0.04 kg m^{-2}. Moreover, the presence of supercooled droplets on top of the cloud (SCT) reduces this positive trend and shows ΔTB (median values) lower than without supercooled droplets (SN) by 1-2 K (40%). When the supercooled droplets are embedded in the cloud (SCE), the trend of ΔTB is similar to the snowfall only (SN) case (similarly to what found over land).

The significance of the results shown in Fig. 9 was also tested by carrying out a statistical test on the Spearman correlation coefficient between 166 ΔTB and SWP, for each manifold, similarly to what was done for the results in Fig. 8. The test confirmed that the positive trends shown in Fig. 9 are significant and represent the trends between the two variables in each manifold, while no trend was evidenced for SCT over sea ice.

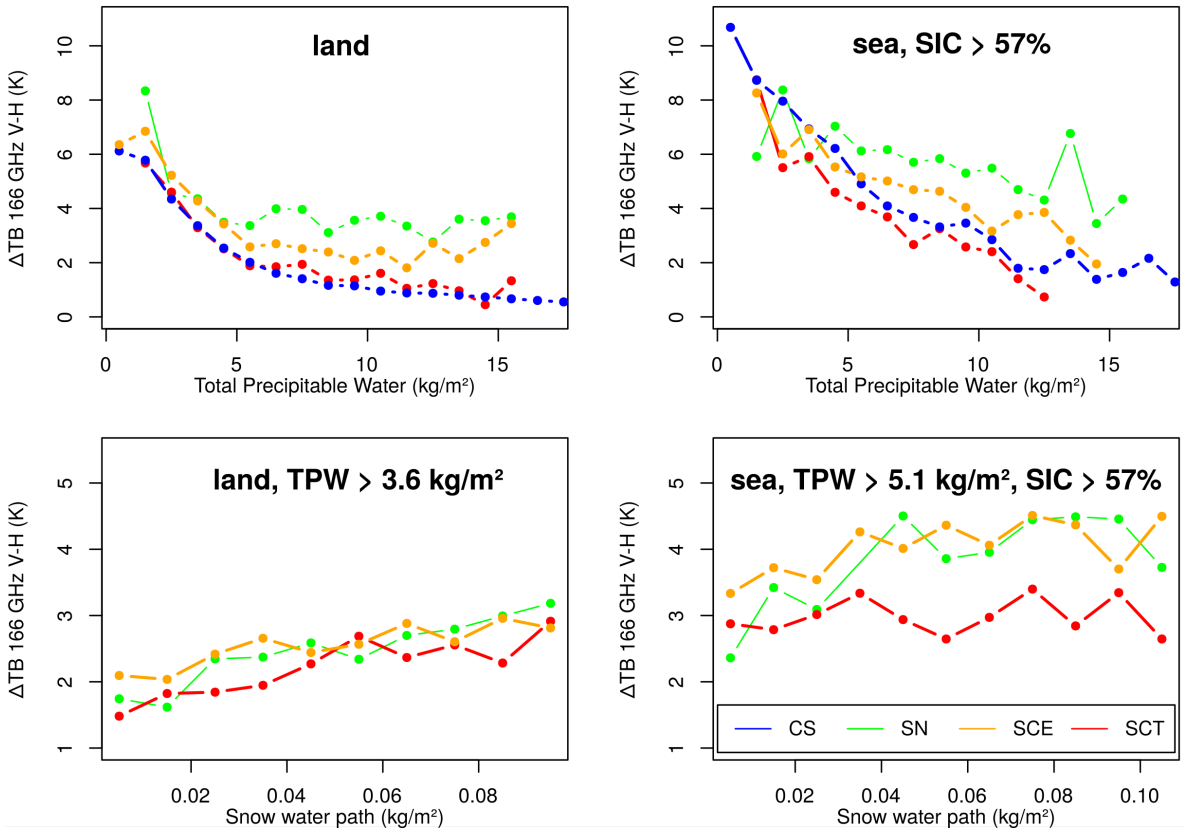

Figure 8. Same as Figure 7 but for 166 GHz ΔTB.

6.4 Discussion

In this study the GMI high-frequency channel response, and in particular the 166 GHz V-pol and H-pol channels, to snowfall is analyzed using CloudSat CPR as a reference. The analysis has been carried out first

considering three case studies, and highlighting very important aspects in the behavior of TBs and ΔTB for the 166 GHz and 183.3 GHz channels under different conditions. Then the analysis of the whole GMI-CPR snowfall dataset allowed to identify quantitatively environmental conditions and cloud properties where 166 ΔTB shows sensitivity to snowfall (detection and amount). Finally, we outlined the complex interconnections between 166 ΔTB and TB with surface type, TPW, SWP, and the presence and vertical distribution of supercooled droplets.

Recent studies using GMI and DPR have highlighted the crucial role of high-frequency channels for snowfall monitoring using microwave radiometer observations (e.g., You et al., 2017, Ebtehaj and Kummerow, 2017). This study focuses on higher latitude snowfall systems because most of the GMI-CPR coincidences occur around 60°N/S, and it includes very weak and/or shallow snowfall systems that are not considered in the study by Ebtehaj and Kummerow (2017) where DPR was used as reference (and therefore, mostly based on more intense snowfall systems). Indeed, as shown in the study carried out during the first part of this FA, and in Casella et al. (2017), DPR detects 5-7% of the global snowfall events with respect to CloudSat, while 29-34% of the global snowfall mass is correctly detected by DPR v4 products. This study also analyzes the behavior of 166 ΔTB (and 183 ΔTB for the case studies) associated with CloudSat-detected snowfall events, following Gong et al. (2017) who analyze global 166 ΔTB signature and find that at higher latitudes the relationship with precipitation is quite complex and requires a dedicated analysis.

TPW and surface type are fundamental parameters needed to determine to what extent GMI TB behavior is related to snowfall. The behavior of ΔTB vs. TB at 166 GHz for the whole dataset evidenced the strong surface/atmosphere contribution to the signal in presence of snowfall because of the lower water vapor contents in winter atmospheres at higher latitudes in the GMI-CPR snowfall dataset compared to the global GMI-DPR dataset used by Gong et al (2017). A very distinct behavior of ΔTB/TB relation has been found for the three different surface types: land, open water, and sea ice. The analysis showed that over land and over sea ice, and for TPW > 3-4 kg m^{-2} and TPW > 5 kg m^{-2} respectively, 166 ΔTB can provide valuable information for snowfall detection and retrieval, while over open water (or low SIC), it is dominated by the polarization by the surface. However, over open water (and to less extent over sea ice), TBs at 166 GHz show a strong dependence on SWP mostly in presence of intense snowfall events and moist conditions (SWP > 0.5 kg m^{-2}, and TPW > 10 kg m^{-2}).

Finally, an analysis of the effect of supercooled water layers on the 166 GHz TBs and ΔTB was undertaken. Our results confirm the results found by Ebtehaj and Kummerow (2017) for snow cover cases during winter. They found that in very cold and dry conditions, with a radiatively cold background surface (i.e., snow-covered land), in presence of snowfall it is possible to have an increase of TBs. Our results show that such an increase may be related to the presence of supercooled droplets, as over land TBs can be up to 10 K higher than snow-only cases because of the supercooled water droplet emission. This effect is also stronger when the droplets are found on top of the ice cloud. In presence of supercooled droplets, 166 GHz TBs therefore do not show a significant trend with the SWP because the cloud droplet emission compensates for the scattering effects by the ice cloud. Similar behavior is observed over sea ice. This effect is noticeable in very dry conditions (TPW < 5 kg m^{-2}). However, 166 ΔTB over land (and sea ice) shows a very distinct trend in presence of snowfall, increasing as SWP increases (for TPW > 3.5 kg m^{-2} over land and for TPW > 5 kg m^{-2} over sea ice). Moreover, over land the depolarization effect at 166 GHz induced by the cloud droplets is on average not enough to eliminate this trend. This shows that ΔTB can be a very valuable parameter to use for snowfall detection for the following difficult circumstances: (1) over land (to a less extent over sea ice), (2) for very weak snowfall events (very low SWP), and (3) for low TPW values in 4-5 kg m^{-2} range.

A few distinct scenarios governed by ambient TPW values were delineated by both analyzing case studies and the entire combined GPM-CloudSat snowfall dataset. First, when snowfall event TPW values are elevated (> 10 kg m^{-2}), the deeper and more intense (e.g., 0-10 dBZ between 6-8 km altitude) the snow-producing cloud needs to have a significant signal at high frequencies. This requirement is due to the fact that as TPW increases, the signal from the cold surface becomes negligible, the weighting function peaks at higher levels, and therefore only thicker clouds (6-8 km) can impact the TBs. Under such circumstances, there is an evident scattering signal at high frequencies (lower 166 GHz and 183.3 GHz TB values with respect to the atmospheric/surface contribution) with a significant 166 GHz polarization signal also visible

(i.e., 166 ΔTB increase). This behavior relates to the spring season findings by Ebtehaj and Kummerow (2017) (presumably characterized by higher TPW), when the atmospheric contribution due to the water vapor is significant, the surface is radiatively warmer, and the snowfall is associated with a high-frequency (166 GHz and 183.3 GHz) TB decrease due to scattering. The presence of supercooled cloud droplets, however, further complicates matters that may hamper the GMI ability to detect snowfall. Shallower clouds (< 5 km cloud top height) do not possess a significant 166 GHz or 183.3 GHz signal. The supercooled cloud droplet emission signal (where present) can be quite significant at 89 GHz, while it is masked by the water vapor contribution at 166 GHz.

For lower TPW values (5 kg m^{-2} < TPW < 10 kg m^{-2}), the high-frequency TB scattering effect is visible for the most intense (Z > 5 dBZ) and deeper clouds (6-8 km), even in the presence of a radiatively cold surface background. 166 ΔTB over land and sea ice can become quite significant in presence of snowfall (> 10 K). This signal is often more evident than the single frequency scattering signal. As TPW decreases further until a 1 kg m^{-2} threshold (snowfall events are extremely rare under this TPW value), the signal from shallower or less intense clouds becomes visible at high GMI frequencies. In the presence of a cold surface background, TBs typically increase with respect to the clear sky, where TBs mainly respond to the radiatively cold snow cover and low emission by water vapor. Such TB increases can be quite significant at 89 GHz, but are less evident at 166 GHz (H-pol channels also display an enhanced signal because the surface emissivity is lower). Once again, these trends relate to the findings by Ebtehaj and Kummerow (2017) that show a TB increase at all frequencies over radiatively cold backgrounds (snow cover) for winter snowfall cases. However, as shown by complementary CALIPSO cloud phase products, such warm/cold contrast of the cloud with respect to the surface is also due to the presence of supercooled droplets.

7. Prototype of a snowfall detection algorithm based on GMI/CPR coincidence dataset

In this section a prototype of a snowfall detection algorithm built from the GMI-CPR coincident dataset is presented to be exploited to enhance future high-latitude PMW precipitation estimates.

The algorithm first needs to characterize the extremely variable background surface for each pixel at the time of the overpass because at high latitudes (especially in cold and dry conditions), high-frequency channels may be affected by the emission and polarization signal from the surface. The GMI low frequency channels can be effectively used to infer information about the background surface (i.e., sea ice concentration, ground, water). Atmospheric water vapor content is also a fundamental variable to be able to determine the atmospheric contribution to the upwelling radiation at the time of the overpass, and to define to what extent high-frequency channel scattering and polarization signal can be related to snowfall.

The frozen surface classification scheme is based on the use of low frequency channels (< 37 GHz, i.e., and 10, 23.8, 18.7, 36.5 GHz TBs. Figure 9 illustrates the flow diagram of the surface classification scheme. Pseudo emissivity for each channels are computed based on the T2m. The algorithms is based on the use of discriminant functions to distinguish snow cover from land surfaces, and to identify the presence of sea ice (see Figure 10 and Figure 11). Sea ice is identified with POD= 0.86 FAR 0.03 (compared to AMSR2 sea ice concentration dataset, SIC > 57%), while snow cover is identidied with POD=0.90 FAR 0.12 (compared to ERA-I snow depth). Moreover, k-mean clusterization method is used to distinguish among different types of snow and sea ice. The sea ice classification is based on the study by Hewison and English (1999) who identified different trends of the emissivity with changing frequency for different types of ice. Three categories of snow cover (A, B, and C) are identified, while sea ice is differentiated between New Ice, First Year Ice (or Broken Ice), and Multilayer Ice.

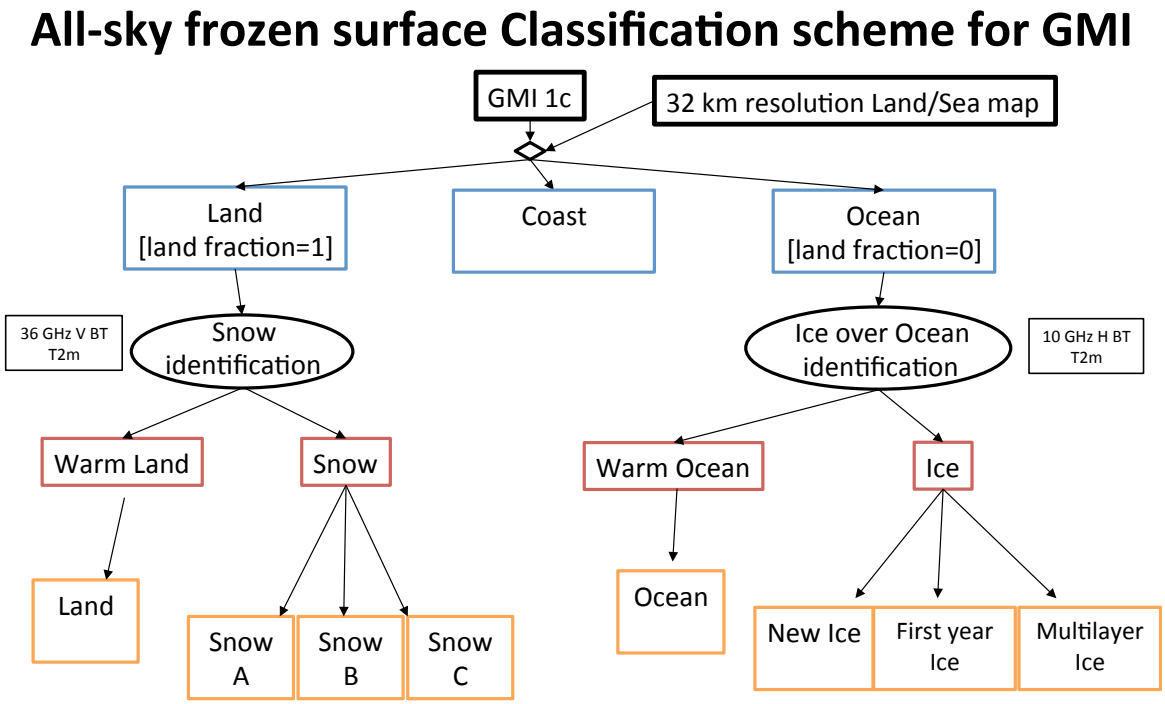

Figure 9: GMI surface classification algorithm flow chart

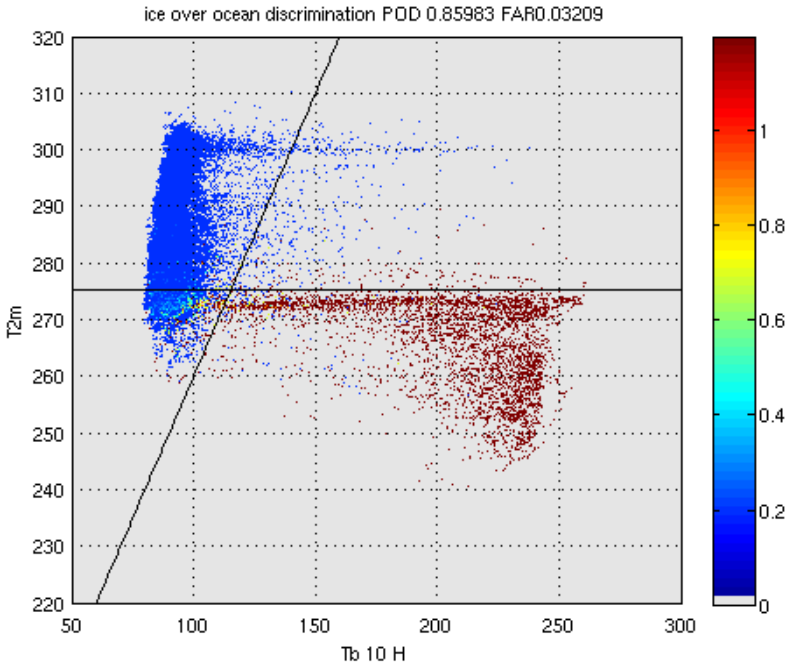

Figure 10: Partitioning of the GMI ocean observations into sea-ice and open sea. Red dots represent sea ice and blue dost represent open sea, as represented in the surface-type variable in the 2C-PRECIP-COLUMN CloudSat product. The black curve represents the discriminant function applied in the GMI classification algorithm.

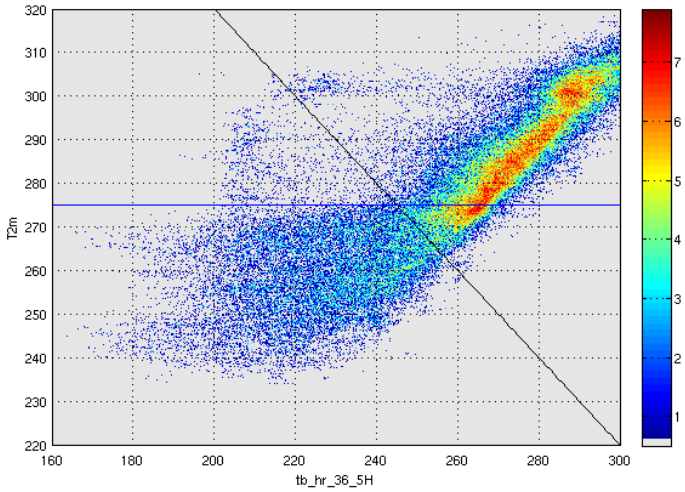

Figure 11: Partitioning of GMI land observations for the snow cover identification. The use of the 36.5 GHz channel and the T2m auxiliary variable of the GMI-CPR dataset are used. The color scale represents the Log10 of the number of occurrences. The black curve represents the discriminant function applied by the algorithm based on snow depth liquid water equivalent as calculated by the ECMWF ERA Interim reanalysis.

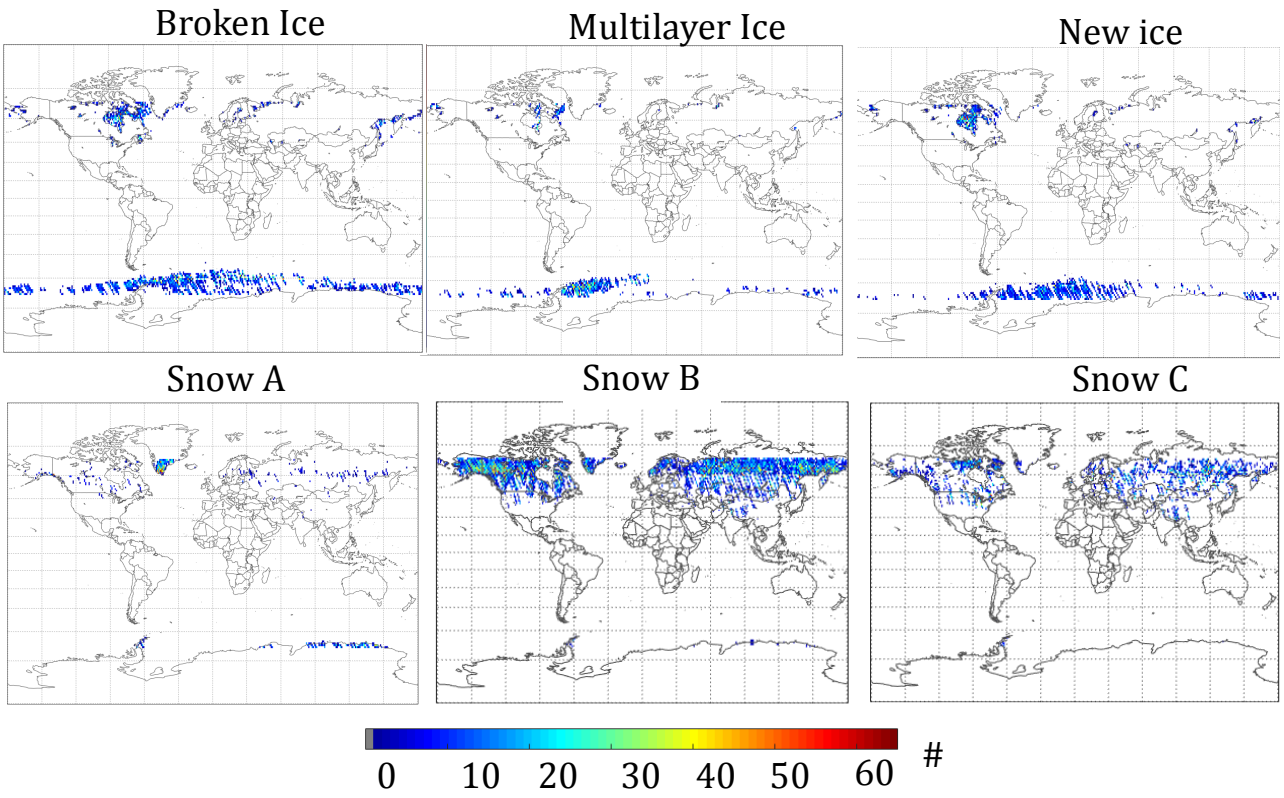

Figure 12: Results of the frozen surface classification scheme for the pixels in the GMI-CPR coincident dataset.

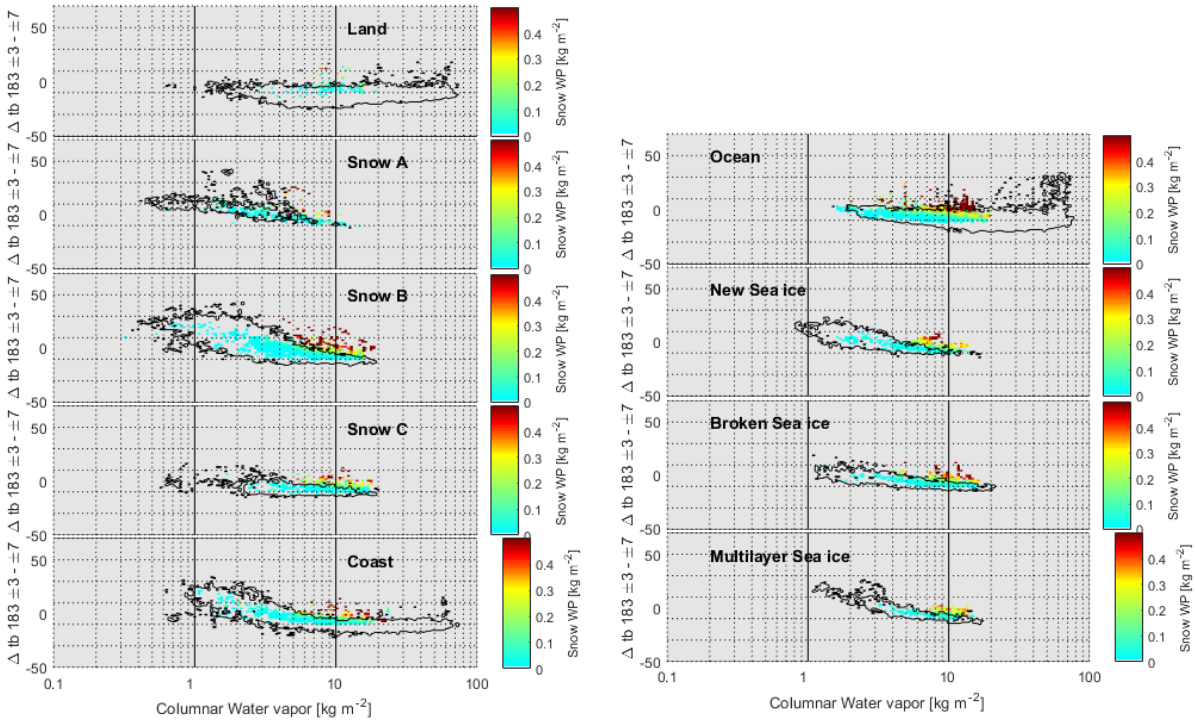

Figure 13: Scatterplots showing the ΔTB183 vs. TPW for all the points in the GMI/CPR coincident dataset and for different surface types. Color scale indicates the SWP as estimated by CloudSat CPR (2C_SNOW product), associated to each point in the dataset with snowfall rate at the surface > 0 mm/h (in 2C-SNOW product SWP is computed when according to the 2C-PRECIP product the snowfall rate at the surface is probable or certain, or if mixed liquid fraction is < 0.1, therefore where CPR snowfall rate at the surface > 0 mm/h). The black contour delineates the manifold for points in the dataset associated to clear sky (i.e., no cloud according to the 2B-CLDCLASS product).

The GMI TB sensitivity to snowfall has been analyzed considering background surface classes found by the syrface classification scheme. Figure 13 shows ΔTB183 values as a function of TPW, with the clear sky manifold indicated by the black contour line (where clear sky is indicated by the 2B-CLDCLASS product). CloudSat derived SWP is also indicated by the color table. Figure 4 indicates that snowfall is associated with a wide range of TPW values (1 kg/m^2 < TPW < 20 kg/m^2) over most surfaces, except for snow A where the maximum TPW is limited to ~10 kg/m^2 (i.e., very dry and cold conditions). Peaks of SWP occur where 5 kg/m^2 < TPW < 20 kg/m^2. Figure 4 clearly indicates that in order to analyze the behavior of ΔTB183 versus SWP, it is necessary to know both TPW and surface type.

For TPW > 5 kg/m^2, as SWP increases ΔTB183 increases with respect to its clear sky values. Over most surfaces this happens for SWP larger than 0.2 kg/m^2, and distinct ΔTB183 signals with respect to clear sky are only observed in this case. The potential to truly detect snowfall events using the ΔTB183 metric is therefore limited to the 0.2 kg/m^2 threshold. The various surface types sometimes display different trends. There are unfortunately very few cases of snowfall over land, or SNOW A, and the majority of events are associated with low SWP. Conversely, there are *many* cases over ocean (open water) associated with large SWP exceeding 0.5 kg/m^2. There is also a very distinct signal of ΔTB183 increase with SWP over broken ice and new sea ice. Lower SWP is associated to multilayer ice, and therefore the ΔTB183 signal is weaker. The largest SWP among all land surfaces are associated with the Snow B category. Correspondingly, there is a distinct signal of ΔTB183 over Snow B, and also Snow C, surfaces.

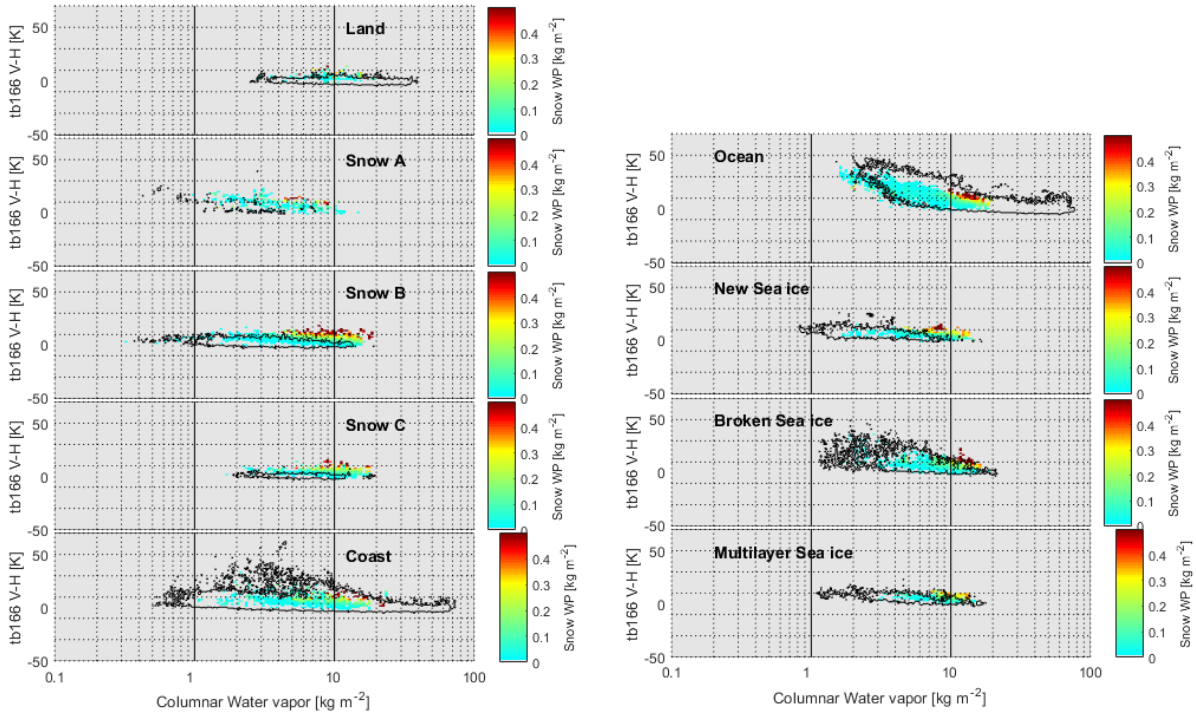

Figure 14: Scatterplots showing the ΔTB166 vs. TPW for all the points in the GMI/CPR coincident dataset and for different surface types. Color scale indicates the SWP as estimated by CloudSat CPR (2C_SNOW product), associated to each point in the dataset with snowfall rate at the surface > 0 mm/h (in 2C-SNOW product SWP is computed when according to the 2C-PRECIP product the snowfall rate at the surface is probable or certain, or if mixed liquid fraction is < 0.1, therefore where CPR snowfall rate at the surface > 0 mm/h). The black contour delineates the manifold for points in the dataset associated to clear sky (i.e., no cloud according to the 2C-CLASS product).

Figure 14 shows similar results as Figure 13, but for ΔTB166 (the 166 GHz V-H difference). Similar to Figure 13, snowfall is associated to 1 kg/m^2 < TPW < 20 kg/m^2 over most surfaces (except for snow A where max TPW is 10 kg/m^2, i.e., very dry and cold conditions). Peaks of SWP occur where 5 kg/m^2 < TPW < 20 kg/m^2. In order to analyze the behavior of ΔTB166 vs. SWP, it is again necessary to know TPW and surface type.

Over most surfaces (except for land, ocean, and Snow A) and for TPW > 5 kg/m^2, as SWP increases ΔTB166 increases with respect to the corresponding values in clear sky. This happens for SWP larger than 0.2 kg/m^2, only in this case we distinguish a distinct signal of ΔTB166 with respect to clear sky. For Snow C and to a less extent for Snow B for TPW > 12 Kg/m^2, we have a distinct snowfall signal also for very low SWP. Again, there are very few cases of snowfall over land, or SNOW A, and they associated with very low SWP values. Over ocean in clear sky we observe large ΔTB166 for low TPW because the TBs are affected by the surface, and ΔTB166 decreases as TPW increases. Over ocean cases associated with large SWP values do not show a distinct signal compared to clear sky. However, we have distinct snowfall occurrence for very low TPW and relatively large ΔTB166. These cases are probably indirectly affected by supercooled droplets lowering ΔTB166 values through the depolarization of the signal from the surface. Finally, there is a very distinct ΔTB166 increase signal with SWP over broken ice and new sea ice for SWP > 0.2 kg/m^2. Lower SWP values are associated with multilayer ice, therefore the ΔTB166 signal is weaker.
For each surface type, GMI-CPR dataset has been divided in bins in terms of ΔTB (at 166 GHz and 183 GHz), and TPW. For each ΔTB/TPW bin the snowfall probability has been computed as the ratio Ns/(Ns+N0) where Ns is number of occurrences of CPR 2C-SNOW surface snowfall rate > 0 mm h-^{1}, and N0 is the number of occurrences without CPR 2C-SNOW surface snowfall.

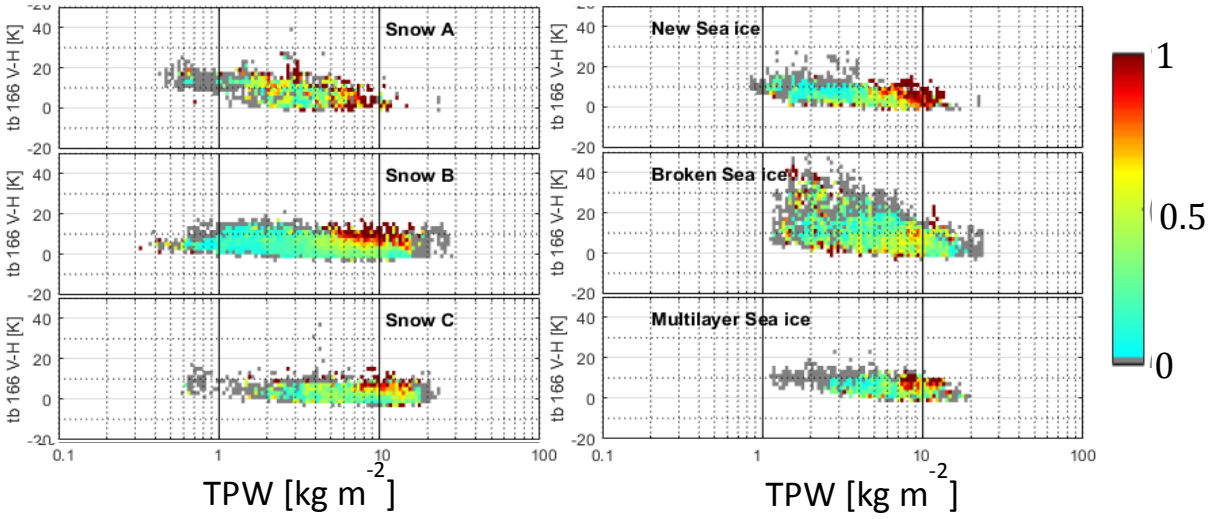

Figure 15: Scatterplots showing snowfall probability (color scale) for all ΔTB166/TPW 2-D bins in the GMI/CPR coincident dataset and for the frozen surface classes. For each surface type, for a given combination (bin) of ΔTB166/TPW snowfall probability is calculated as Ns/(Ns+N0) where Ns is number of occurrences of CPR 2C-SNOW surface snowfall rate > 0 mm/h, N0 occurrences without CPR 2C-SNOW surface snowfall.

The analysis shows good sensitivity to snowfall of 166ΔTB over most surfaces. Over Snow B, Snow C and New Sea Ice, snowfall probability is larger when TPW > 5 kg/m^2 (confirming the results found in Section 6.2). For Snow B and Snow C the largest probabilities are associated with larger 166 ΔTB. For New Sea Ice, large snowfall probabilities are associated with 166 ΔTB < 10 K. Over Multilayer Sea Ice, larger probabilities occur for TPW > 8 kg/m^2. In these cases, higher probabilities are associated with higher ΔTB166 (around 10 K). Very light snowfall is associated to Snow A. Over Broken ice (and over ocean) 166 ΔTB is not very effective because of the high polarization signal due to the surface. On the other hand, 183ΔTB shows sensitivity to snowfall over Broken sea Ice (and over Ocean, not shown), and lower sensitivity then 166 ΔTB over snow cover. The combined use of 183ΔTB and 166ΔTB can be very effective for snowfall detection over all frozen surface types, while the 183 Ghz channels are very useful over ocean (and broken sea ice) .

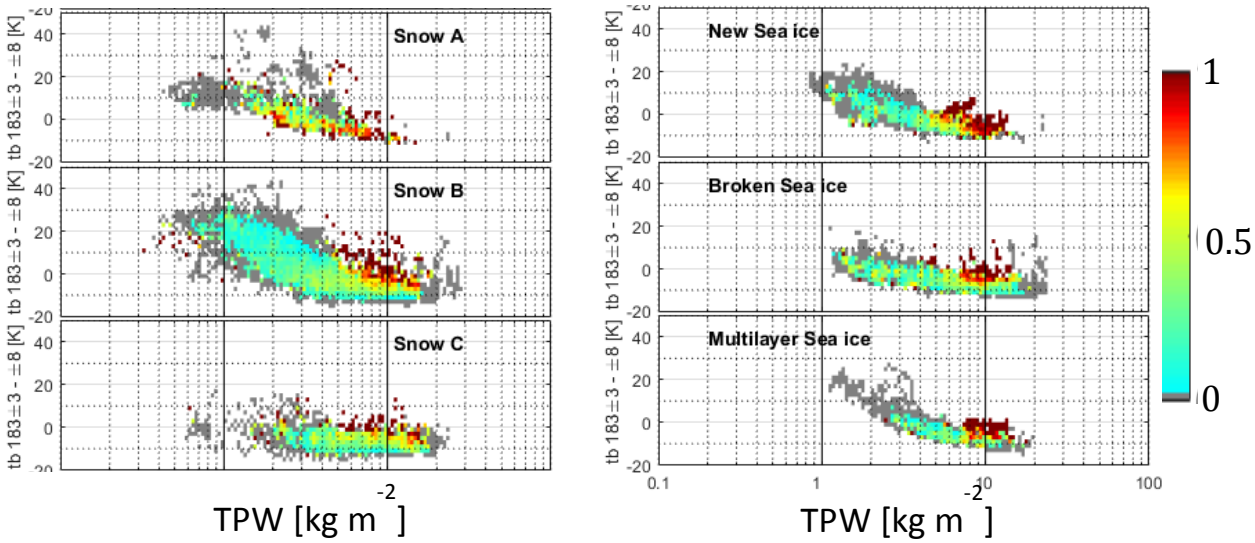

Figure 16: Scatterplots showing snowfall probability (color scale) for all ΔTB183/TPW 2-D bins in the GMI/CPR coincident dataset and for the frozen surface classes. For each surface type, for a given combination (bin) of ΔTB183/TPW snowfall probability is calculated as Ns/(Ns+N0) where Ns is number of occurrences of CPR 2C-SNOW surface snowfall rate > 0 mm/h, N0 occurrences without CPR 2C-SNOW surface snowfall.

	Ocean	New Sea ice	Broken Sea ice	Multilayer Sea ice	Coast	Snow A	Snow B	Snow C
# of snow pixels/total	1919/ 23664	120/3 36	454/ 1123	58/ 180	72/ 2195	32/ 62	85/ 353	111/ 291
POD	0.80	0.60	0.83	0.72	0.74	0.31	0.54	0.74
FAR	0.40	0.35	0.47	0.54	0.37	0.09	0.36	0.49

Table 2: Results of snowfall detection scheme with indipendent GMI/CPR dataset June-Dec. 2016. For each surface type the value of the probability of snowfall that maximizes the HSS in the training dataset is selected as the value to evaluate the snowfall detection capabilities.

Based on the results shown in Section 6.2, and in Figure 13 and 14, a look-up table scheme has been developed to be able to compute snowfall probability for each GMI pixel a the time of each overpass. The scheme is based on two steps:

1) Preliminary probability of snowfall is based on a 3-D look-up table built from environmental variables (following Sims and Liu, 2015]:

TPW (50 bins, linear scale)

T2m (50 bins, log scale)

Lapse rate 2-500 m (20 bins, linear scale)

The full 6-years global CPR database (2006-2011) (day and night overpasses) has been used to build the 3-D look-up table.

2) If preliminary probability of snowfall based on 1) is higher than 10% the probability of snowfall is computed based on a 4-D look-up table built upon:

Surface type

TPW

ΔTB at 166 GHz (V-H)

ΔTB at 183.3 GHz (183±3 -183±7 GHz)

The GMI/CPR coincident observation dataset (March 2014-May 2016) has been used to build the 4-D look-up table. For each bin (either for the 3-D or for the 4-D look up table), the probability of snowfall is computed as Ns/(Ns+N0), where Ns is number of occurrences of CPR 2C-SNOW surface snowfall rate > 0 mm h^{-1}, and N0 is the number of occurrences without CPR 2C-SNOW surface snowfall.
The look-up table scheme has been applied to an independent dataset built from GMI-CPR coincidences (June-Dec. 2016). Since the 2C-SNOW product was not available for this time frame, snowfall occurrences have been validated against the 2C-PRECIP product phase flags, using the same criteria used in the 2C-SNOW: precipitation Flag equal to Snow Possible or Certain, or Mixed Precipitation with liquid fraction < 10%. For each surface type the value of the probability of snowfall that maximizes the HSS in the training dataset is selected as the value to evaluate the snowfall detection capabilities. Table 2 shows the results of the snowfall detection scheme for the different surface types. The results are affected by the small sample size. The high POD found over most surfaces (in particular over broken sea ice, snow C, and ocean) shows that look-up tables built from the GMI-CPR observational dataset have good potentials and could be exploited towards the development of snowfall detection schemes to be implemented in the currently available precipitation retrieval algorithms. However, the high FAR highlights the difficulties associated with isolating the snowfall signal at higher microwave frequencies due to complex interaction between surface and atmospheric features (TPW, presence of supercooled droplets) that determine the multi-frequency TB signal. Further development is foreseen where more sophisticated techniques (e.g., regression tree analysis) may be used to find the optimal set of parameters (including single channel TBs at high frequencies) best correlated with snowfall for each surface type, to be exploited in snowfall retrieval

algorithms. Further analysis will be carried out when a larger independent CPR snowfall dataset will be available, and results will be compared to currently available GMI snowfall products (e.g., GPROF).

8. Modeling the optical properties of ice clouds in the MW spectrum: challenges and recommendations

A last important task of the FA was to dedicated to exploit the expertise, tool, and datasets available through the PMM Science Team towards the improvement of the representation of the optical properties model of ice clouds at microwave frequencies. The widely used homogeneous soft spherical approximation for the single scattering properties of ice crystals has been questioned by several authors (e.g., Ishimoto, H., 2008, Kulie et al., 2010, Petty and Huang, 2010, Tyynela et al., 2010, Leinone et al., 2012). Several studies attempted to describe the properties of more realistic, nonspherical pristine ice crystals and aggregates of crystals (e.g., Liu , 2004, Kim, 2006, Weinman and Kim, 2007, Botta and Aydin, 2010, Ori et al., 2014, Johnson et al., 2012, 2016, Kulie et al., 2014, Kuo et al., 2016) using different methods such as the discrete dipole approximation (DDA) (Draine and Flatau, 1994, 2013). The OpenSSP database (Kuo et al., 2016), made available through the NASA PPS of the PMM Research Program, represents the most advanced and complete database of ice single scattering properties available. OpenSSP is built by 9 pristine crystals habits (various dendrites, needles, and sandwich plates); pristine crystals were generated using a 3D growth model, and these crystals were aggregated using a self-collection algorithm to create a large set (6646) of snow particles (generically defined complex geometric frozen hydrometeors ranging from single dendritic snowflakes to aggregates comprised of a possible variety of pristine ice crystals. On the other hand, in Hong (2007) and Hong et al. (2009) 6 habits of pristine ice crystals have been simulated in the frequency range between 89 and 1000 GHz.
The Kulie et al. (2010) and Hiley et al. (2011) methodology (hereafter KH model), deriving the optical properties of ice cloud (with and without falling snow) starting from the CloudSat CPR reflectivity profiles, has been implemented at CNR-ISAC. Moreover, the KH model has been coupled with the OpenSSP single scattering tables for not-spherical ice crystals, including complex snowflakes and aggregates. The model simulates absorption and extinction coefficient, single scattering albedo, asymmetry factor, and backscatter cross-section. The simulation of TBs for the channels of the currently available radiometers, as well as for the EPS-SG MWS, MWI sensors , and W-band (CPR) and Ka- Ku-band (DPR) reflectivities will be a further step to be accomplished within the ongoing collaboration with the PMM Science Team.
The OpenSSP database includes particles with radius as large as 14 mm, at frequencies as high as 183 GHz. Moreover, it does not cover some important aspects:

- Modeling of other pristine crystals habits considered by other authors;
- Riming of ice crystals;
- Partially melted hydrometeors.

Therefore, there are several areas of improvements and further development in the SSP modelization for applications in PMW precipitation retrieval, in particular for the future EPS-SG radiometers (MWI, MWS, and ICI, with frequency up to 664 GHz). Among these it is worth mentioning:

1- To calculate the scattering properties of ice particles (pristine ice crystals and snow) in the OpenSSP database for all frequencies that are not already included useful for the the EPS-SG mission (MWI, MWS and ICI).

2- To extend the resulting SSP database to a larger set of pristine ice crystal habits considering also the 6 habits defined by Hong (2007) and Hong et al. (2009).

3- To include in the new database partially rimed crystals and graupel.

4- To enlarge this database including partially melted hydrometeors.

5- To define ice particle ensembles made of homogeneous habit, orientation and size, to create an optimized database for implementation in radiative transfer models.

It is also recommended to carry out sensitivity studies aimed at assessing the impact on the SSP of temperature, index of refraction, and number of orientation angles with respect to other ice particle characteristics (e.g., shape).

The use of DDA poses some challenges in terms of the computational needs to accomplish these tasks. In DDA, the target object is approximated as an array of polarizable points that are on a cubic lattice. The polarizable points acquire dipole moments via their response to the local electric field and the electric fields of surrounding points. This method requires that the spacing between dipoles must be sufficiently small compared to the interacting electromagnetic wavelength determined from the relationship $m|(k*d)$<0.5 (Draine and Flatau, 2013) where *m* is the complex index of refraction, *k* is the wavenumber, and *d* is the dipole spacing. This implies the use of a lattice whose axis size dimensions are:

$$N > \frac{2r}{d}$$

where *r* is the maximum dimension of the ice particle to be simulated, e.g., at 664 GHz (λ=451 μm, d≤ 20 μm) 1 mm radius particle requires 1 million of dipoles to be correctly simulated using DDA. Considering that the computation time of DDA follows roughly the exponential rule (Draine and Flatau, 2013):

$$CPU_{time} \sim 10^{log_2(N)}$$

by doubling N the computation time becomes 10 times longer, or, in other terms, the calculation of the SSP of the same ice particle is 100 times longer at 664 GHz than at 183 GHz. In order to limit the computation time needed DDA simulations particle radius could be limited to 8 mm for frequencies higher than 300 GHz. The SSP results will have to be stored for every ice crystal realization for every orientation considered, allowing the calculation of randomly oriented particles and of preferentially oriented particles. Johnson et al. (2016) assume that 75 orientations are sufficient in order to calculate the SSP for randomly oriented particles. Considering the observation angle of 53° for EPS-SG ICI and MWI and between ±50° for MWS, the SSP could be computed for 17 orientations w.r.t. the nadir angle (15 from 0° to 90° spaced by 6°, plus ±53°) and for 5 orientations in the azimuth angle (from 0° to 360° spaced by 24°). Sensitivity studies are recommended to establish the number of orientations to be considered.

For the definition of the rimed particles, different level of riming may be considered following the Casella et al. (2008) methodology. Rimed ice realizations should also include some conic graupel and lump graupel. The partially melted hydrometeors can be defined selecting from the pristine crystals, snow/aggregates, and rimed particles, and adopting the Johnson et al. (2016) scheme, considering different levels of melting.

9. Conclusions

This Final Report illustrates case study analyses from a matched GMI-CPR dataset that provides instructive insights to highlight widely varying GMI multi-frequency signals associated with different snowfall types. The case study results are followed by an aggregated TB response analysis of the entire GMI-CPR dataset aimed at showing the behavior of GMI channels in presence of snowfall under different environmental conditions. In addition, the study exploits CloudSat products to investigate the impact of supercooled cloud droplets on the GMI observations of snowfall in relation to the environmental conditions and cloud characteristics. A prototype snowfall detection scheme based on look-up tables built from the main findings of this study is also presented, but further development of snowfall detection and retrieval scheme is foreseen in the current H-SAF phase (CDOP-3). The results of this Final Report need to be considered jointly with the results presented in the Mid-term Report where the GPM DPR and ATMS snowfall detection capabilities were analyzed.

The ultimate goal of this FA was to provide some quantitative criteria and guidelines derived from the complex relations between GMI and ATMS observations and snowfall at higher latitudes to be exploited in the development of a snowfall detection algorithm for current and future microwave radiometers. The

work carried out in this FA demonstrates the great potential of combined spaceborne radiometer-radar observational dataset to define microwave radiometer snowfall detection limitations and capabilities. It is important to consider that the most accurate and up to date CloudSat/CALIPSO/ECMWF snowfall-related products have been used in this work. These products are subject to uncertainties whose assessments are worthy of separate exhaustive investigations. However, based on previous studies and on a critical analysis of our results, we deem that these uncertainties are limited enough to obtain meaningful insights from the analysis shown. For snowfall, it is essential to be able to characterize key environmental characteristics (i.e., background surface, sea ice concentration, and total precipitable water).

All components of this FA, and the results presented in this Final Report, ultimately improve our ability to interpret passive microwave observations associated with a diverse set of snowfall events comprised of different cloud microphysical and macrophysical properties and associated with varying environmental conditions. They also demonstrates that the use of observational datasets built from coincident spaceborne radar and radiometer observations can contribute significantly to overcome some of the limitations of the representativeness of cloud-radiation model simulations, in particular at the high frequency channels used for light precipitation and snowfall retrieval. However, the correct modelization of the ice cloud optical properties in the microwave spectrum (particularly challenging at high frequency) is at the base of the development of passive microwave retrieval algorithms, especially for future radiometers with channel assortment and viewing geometry different from what is currently available. A winning strategy for the refinement of snowfall and light precipitation retrieval techniques, relying on the use of high frequency channels, would be to combine the use of the observational datasets with the refinement of the physical assumptions in the generation of the cloud-radiation model databases. In Section 8 the state-of-the-art, the important challenges, and recommendations in the ice cloud optical properties modelization for PMW precipitation retrieval applications (also in view of the EPS-SG mission), have been presented.

The main results of this FA have been presented at the 8th IPWG- 5th IWSSM Joint Workshop (Bologna, Italy, October 2016), at the 2017 EGU General Assembly (Vienna, Austria, 2017), at the First Snowfall Workshop (Cologne, Germany, June 2017), at the PMM Science Team meeting (San Diego, USA, October 2017), and at the EUMETSAT Conference (Rome, Italy, October 2017) and have been collected in two peer-reviewed articles (Casella et al., 2017, Panegrossi et al., 2017). Two additional papers on the GMI and ATMS surface classification schemes and GMI snowfall detection scheme are in preparation.

It is worth noting that this FA, and the fruitful interaction between scientists in the H-SAF and in the PMM communities throughout the CDOP-2 (and CDOP-3) has been very beneficial also in view of the future phases of the SAF program, aimed at the delivery of advanced precipitation (and cloud) products for the EPS-SG equipped with the cross-track scanning radiometer MWS, and the conically scanning radiometers MWI, and ICI. This interaction will reinforce the important role of the EUMETSAT H-SAF in the delivery of operational satellite-based precipitation products.

Acknowledgements

The datasets used in this study have been collected from the NASA PPS website ftp://arthurhou.pps.eosdis.nasa.gov (GPM products, 2B-CSATGPM product), from the CloudSat website ftp.cloudsat.cira.colostate.edu (CPR products), from http://www.icare.univ-lille1.fr/projects/dardar (DARDAR product), and from https://seaice.uni-bremen.de/sea-ice-concentration/ (AMSR2 sea ice dataset). The H-SAF Science Management, in particular Capt. Davide Melfi and Stefano Dietrich, is acknowledged for supporting the Federated Activity H_SAF_FA15_01. The PMM Research Program and EUMETSAT are acknowledged for supporting and endorsing the H-SAF and GPM collaboration through the approval of the no-cost scientific proposal “H-SAF and GPM: precipitation algorithm development and validation activity”. Joe Turk is warmly acknowledged for developing and sharing the 2B-CSATGPM dataset used in this study, and Norm Wood for the valuable discussions and suggestions on the use of the CloudSat 2C-SNOW-profile product.

References

Behrangi, A., M. Christensen, M. Richardson, M. Lebsock, G. Stephens, G. J. Huffman, D. Bolvin, R. F. Adler, A. Gardner, B. Lambrigtsen, and E. Fetzer, 2016: Status of high-latitude precipitation estimates from observations and reanalyses. *J. Geophys. Res. Atmos.*, 121, 4468-4486, doi: 10.1002/2015JD024546.

Bennartz R., and P. Bauer, 2003: Sensitivity of microwave radiances at 85–183 GHz to precipitating ice particles, *Radio Sci.,* 38 (4), 8075, doi:10.1029/2002RS002626.

Bennartz, R., and G. W. Petty, 2001: The sensitivity of microwave remote sensing observations of precipitation to ice particle size distributions. *J. Appl. Meteor.,* 40, 345-364.

Boening, C., M. Lebsock, F. Landerer, and G. Stephens, 2012: Snowfall-driven mass change on the East Antarctic ice sheet. *Geophys. Res. Lett.*, 39(21).

Botta, G., and K. Aydin, 2010: Modeling of microwave scattering from cloud ice crystal aggregates and melting aggregates: A new approach. *IEEE Trans. Geosci. Remote Sens. Lett.*, **7**, 572-576.

Casella D., Mugnai A, Sanò P., Formenton M.: Microwave single-scattering properties of randomly oriented soft-ice hydrometeors. Adv. Geosci., 17; 79-85, ISSN: 1680-7340, 2008

Casella, D., G. Panegrossi, P. Sanò, A. C. Marra, S. Dietrich, B. T. Johnson, and M. S. Kulie, 2017: Evaluation of the GPM-DPM snowfall detection capability: Comparison with CloudSat-CPR. *Atmos. Res*., 2017, *197*, 64–75, doi:10.1016/j.atmosres.2017.06.018.

Chen, S.; Hong, Y.; Kulie, M.; Behrangi, A.; Stepanian, P. M.; Cao, Q.; You, Y.; Zhang, J.; Hu, J.; Zhang, X. Comparison of snowfall estimates from the NASA CloudSat Cloud Profiling Radar and NOAA/NSSL Multi-Radar Multi-Sensor System. *J. Hydrol.* 2016, *3644*, doi:10.1016/j.jhydrol.2016.07.047.

Delanoë, J.; Hogan, R. J. A variational scheme for retrieving ice cloud properties from combined radar, lidar, and infrared radiometer. *J. Geophys. Res.* 2008, *113*, doi:10.1029/2007JD009000.

Delanoë, J.; Hogan, R. J. Combined CloudSat-CALIPSO-MODIS retrievals of the properties of ice clouds. *J. Geophys. Res.* 2010, *115*, doi:10.1029/2009JD012346.

Di Michele, S., and P. Bauer, 2006: Passive microwave radiometer channel selection based on cloud and precipitation information content. *Quart. J. Roy. Meteor. Soc*., 132, 1299–1323, doi:10.1256/qj.05.164.

Draine, B. T., and P. J. Flatau, 1994: Discrete dipole approximation for scattering calculations. *J. Opt. Soc. Am*., **A11**, 1491-1499.

Draine, B. T., and P. J. Flatau, 2013: User Guide for the Discrete Dipole Approximation Code DDSCAT 7.3 http://ddscat.wdfiles.com/local--files/downloads/ddscat7.3.0_UserGuide_130529.pdf

Ebtehaj, A. M.; Kummerow, C. D. Microwave retrievals of terrestrial precipitation over snow-covered surfaces: A lesson from the GPM satellite. *Geophys. Res. Lett.* 2017, *44*, 6154–6162, doi:10.1002/2017GL073451.

Gong, J.; Wu, D. L. Microphysical properties of frozen particles inferred from Global Precipitation Measurement (GPM) Microwave Imager (GMI) polarimetric measurements. *Atmospheric Chem. Phys.* 2017, *17*, 2741–2757, doi:10.5194/acp-17-2741-2017.

Grecu, M.; Olson, W. S.; Munchak, S. J.; Ringerud, S.; Liao, L.; Haddad, Z.; Kelley, B. L.; McLaughlin, S. F. The GPM Combined Algorithm. *J. Atmospheric Ocean. Technol.* 2016, *33*, 2225–2245, doi:10.1175/JTECH-D-16-0019.1.

Hiley, M. J.; Kulie, M. S.; Bennartz, R. Uncertainty analysis for CloudSat snowfall retrievals. *J. Appl. Meteorol. Climatol.* 2011, *50*, 399–418, doi:10.1175/2010JAMC2505.1.

Hong, G. (2007), Parameterization of scattering and absorption properties of nonspherical ice crystals at microwave frequencies, J. Geophys. Res., 112, D11208, doi:10.1029/2006JD008364

Iguchi, T.; Seto, S.; Meneghini, R.; Yoshida, N.; Awaka, J.; Kubota, T. GPM/DPR Level -2 Algorithm Theoretical Basis Document 2016.

Ishimoto, H., 2008: Radar backscattering computations for fractal-shaped snowflakes. *J. Meteor. Soc. Japan*, **86**, 459-469.

Johnson, B.T., Petty, G. W., Skofronick-Jackson, G. S., 2012: Microwave Properties of Ice-Phase Hydrometeors for Radar and Radiometers: Sensitivity to Model Assumptions. Journal of Applied Meteorology and Climatology, 51(12), 2152–2171.

Johnson, B.T., Olson, W.S. and Skofronick-Jackson, G., 2016. The microwave properties of simulated melting precipitation particles: sensitivity to initial melting. *Atmospheric Measurement Techniques*, 9, 9-21, doi:10.5194/amt-9-9-2016.

Kim, M.-J., 2006: Single scattering parameters of randomly oriented snow particles at microwave frequencies. J. Geophys. Res. Atmos., 111, D14201, doi:10.1029/2005JD006892.

Kneifel, S.; Löhnert, U.; Battaglia, A.; Crewell, S.; Siebler, D. Snow scattering signals in ground-based passive microwave radiometer measurements. *J. Geophys. Res.* 2010, *115*, doi:10.1029/2010JD013856.

Kongoli, C., P. Pellegrino, R. R. Ferraro, N. C. Grody, and H. Meng, 2003: A new snowfall detection algorithm over land using measurements from the Advanced Microwave Sounding Unit (AMSU). *Geophys. Res. Lett*., 30, 1756, doi:10.1029/2003GL017177.

Kongoli, C., H. Meng, J. Dong, and R. Ferraro, 2015: A snowfall detection algorithm over land utilizing high-frequency passive microwave measurements—Application to ATMS. *J. Geophys. Res. Atmos*., 120, 1918–1932, doi:10.1002/2014JD022427.

Kulie, M. S., and R. Bennartz, 2009: Utilizing spaceborne radars to retrieve dry snowfall. *J Appl Meteor Clim*, 48, 2564-2580.

Kulie, M. S., R. Bennartz, T. J. Greenwald, Y. Chen, and F. Z. Weng, 2010: Uncertainties in microwave properties of frozen precipitation: Implications for remote sensing and data assimilation. *J Atmos Sci*, 67, 3471-3487.

Kulie, M. S., M. J. Hiley, R. Bennartz, S. Kneifel, and S. Tanelli, 2014: Triple-frequency radar reflectivity signatures of snow: Observations and comparisons with theoretical ice particle scattering models. *J. Appl. Meteor. and Climatol.*, **53**, 1080-1098.

Kulie, M. S., 2016: A shallow cumuliform snowfall census using spaceborne radar. *J. Hydrometeor*., 17, 1261-1279. doi: 10.1175/JHM-D-15-0123.1

Kummerow, C. D., D. L. Randel, M. Kulie, N.-Y. Wang, R. Ferraro, S. J. Munchak, and V. Petkovic, 2015: The evolution of the Goddard Profiling Algorithm to a fully parametric scheme. *J. Atmos. Oceanic Technol.*, 32, 2265–2280. doi: http://dx.doi.org/10.1175/JTECH-D-15-0039.1

Kuo, K., W.S. Olson, B.T. Johnson, M. Grecu, L. Tian, T.L. Clune, B.H. van Aartsen, A.J. Heymsfield, L. Liao, and R. Meneghini, 2016: The microwave radiative properties of falling snow derived from nonspherical ice particle models. Part I: An extensive database of simulated pristine crystals and aggregate particles and their scattering properties *J. Appl. Meteor. Climatol.,* 55, 691–708, doi: 10.1175/JAMC-D-15-130.1.

L'Ecuyer, T. S.; Jiang, J. H. Touring the atmosphere aboard the A-Train. *Phys. Today* 2010, *63*, 36–41, doi:10.1063/1.3463626.

Leinonen, J., S. Kneifel, D. Moisseev, J. Tyynela, S. Tanelli, and T. Nousiainen, 2012: Evidence of nonspheroidal behavior in millimeter-wavelength radar observations of snowfall. *J. Geophys. Res.*, **117**, D18205, doi:10.1029/2012JD017680.

Liu, G., 2004: Approximation of single scattering properties of ice and snow particles for high microwave frequencies. J. Atmos. Sci., 61, 2441-2456.

Liu, G., 2008: Deriving snow cloud characteristics from CloudSat observations. *J. Geophys. Res.*, 113, D00A09, doi:10.1029/ 2007JD009766.

Liu, G.; Seo, E.-K. Detecting snowfall over land by satellite high-frequency microwave observations: The lack of scattering signature and a statistical approach. *J. Geophys. Res. Atmospheres* 2013, *118*, 1376–1387, doi:10.1002/jgrd.50172.

Milani, L.; Kulie, M. S.; Casella, D.; Dietrich, S.; L'Ecuyer, T. S.; Panegrossi, G.; Porcù, F.; Sanò, P.; Wood, N. B. CloudSat Snowfall Estimates over Antarctica and the Southern Ocean: An Assessment of Independent Retrieval Methodologies and Multi-Year Snowfall Analysis. *Atmospheric Res.* under review.

Noh, Y.-J., G. Liu, A. S. Jones, and T. H. Vonder Haar, 2009: Toward snowfall retrieval over land by combining satellite and in situ measurements. *J. Geophys. Res*., 114, D24205, doi:10.1029/2009JD012307.

Olson, W.S., L. Tian, M. Grecu, K. Kuo, B.T. Johnson, A.J. Heymsfield, A. Bansemer, G.M. Heymsfield, J.R. Wang, and R. Meneghini, 2016: The microwave radiative properties of falling snow derived from nonspherical ice particle models. Part II: Initial testing using radar, radiometer and in situ observations. *J. Appl. Meteor. Climatol.,* 55, 709–722, doi: 10.1175/JAMC-D-15-0131.1

Ori, D., T. Maestri, R 743 . Rizzi, D. Cimini, M. Montopoli, and F. S. Marzano, 2014: Scattering properties of modeled complex snowflakes and mixed-phase particles at microwave and millimeter frequencies. J. Geophys. Res. Atmos., 119, 9931-9947.

Panegrossi G., J-F. Rysman, D. Casella, A. C. Marra, P. Sanò, and M. S. Kulie, 2017: CloudSat-based assessment of GPM Microwave Imager snowfall observation capabilities, Rem. Sensing, *under review.*

Palerme, C.; Kay, J. E.; Genthon, C.; L'Ecuyer, T.; Wood, N. B.; Claud, C. How much snow falls on the Antarctic ice sheet? *The Cryosphere* 2014, *8*, 1577–1587, doi:10.5194/tc-8-1577-2014.

Petty, G. W., 1994: Physical retrievals of over-ocean rain rate from multichannel microwave imagery. Part 1: Theoretical characteristics of normalized polarization and scattering indexes. *Meteorology and Atmospheric Physics,* 54, 79-99.

Petty, G. W., and W. Huang, 2010: Microwave backscattering and extinction by soft ice spheres and complex snow aggregates. *J. Atmos. Sci.*, **67**, 769-787.

Prigent, C., F. Aires, and W. Rossow, 2006: Land surface microwave emissivities over the globe for a decade. *Bull. Amer. Meteor. Soc*., 87, 1573–1584, doi:10.1175/BAMS-87-11-1573.

Skofronick-Jackson, G,M.-J. Kim, J. A. Weinman, and D.-E. Chang, 2004:A physical model to determine snowfall over land by microwave radiometry. *IEEE Trans. Geosci. Remote Sens*., 42, 1047–1058, doi:10.1109/TGRS.2004.825585.

Skofronick-Jackson, G., and B. T. Johnson, 2011: Surface and atmospheric contributions to passive microwave brightness temperatures for falling snow events. *J. Geophys. Res*., 116, D02213, doi:10.1029/2010JD014438.

Spencer, R.W., H.M. Goodman, and R.E. Hood, 1989: Precipitation retrieval over land and ocean with the SSM/I: Identification and characteristics of the scattering signal. *J. Atmos. Oceanic Technol.*, 6, 254–273.

Surussavadee, C., and D. H. Staelin, 2009: Satellite retrievals of arctic and equatorial rain and snowfall rates using millimeter wavelengths. IEEE Trans. Geosci. Remote Sens., 47, 3697–3707, doi:10.1109/TGRS.2009.2029093.

Turk, F. J., Z. S. Haddad, and Y. You, 2014: Principal components of multifrequency microwave land surface emissivities. Part I: Estimation under clear and precipitating conditions. *J. Hydrometeor*., 15, 3–19, doi:10.1175/JHM-D-13-08.1.

Turk, F. J. CloudSat-GPM Coincidence Dataset 2016.

Tyynela, J., J. Leinonen, D. Moisseev, and T. Nousiainen, 2011: Radar backscattering from snowflakes: comparison of fractal, aggregate, and soft spheroid models. *J. Atmos. Oceanic Technol.*, **28**, 1365-1372.

Wang, Y.; Liu, G.; Seo, E.-K.; Fu, Y. Liquid water in snowing clouds: Implications for satellite remote sensing of snowfall. *Atmospheric Res.* 2013, *131*, 60–72, doi:10.1016/j.atmosres.2012.06.008.

Weinman, J. A., and M.-J. Kim, 2007: A simple model of the millimeter-wave scattering parameters of randomly oriented aggregates of finite cylindrical ice hydrometeors. J. Atmos. Sci., 64, 634-644.

Wood, N. B.; L'Ecuyer, T. S.; Bliven, F. L.; Stephens, G. L. Characterization of video disdrometer uncertainties and impacts on estimates of snowfall rate and radar reflectivity. *Atmospheric Meas. Tech.* 2013, *6*, 3635–3648, doi:10.5194/amt-6-3635-2013.

Wood, N. B.; L'Ecuyer, T. S.; Heymsfield, A. J.; Stephens, G. L.; Hudak, D. R.; Rodriguez, P. Estimating snow microphysical properties using collocated multisensor observations. *J. Geophys. Res. Atmospheres* 2014, *119*, 8941–8961, doi:10.1002/2013JD021303.

Xie, X.; Löhnert, U.; Kneifel, S.; Crewell, S. Snow particle orientation observed by ground-based microwave radiometry. *J. Geophys. Res. Atmospheres* 2012, *117*, n/a-n/a, doi:10.1029/2011JD016369.

You, Y., N. Y. Wang, R. Ferraro, and S. Rudlosky, 2017: Quantifying the Snowfall Detection Performance of the GPM Microwave Imager Channels over Land. *J. Hydrometeor.*, 729-751, doi: 10.1175/JHM-D-16-0190.1.